Supporting Information

La^{III} and Zn^{II} Cooperatively Template a Metal-Organic Capsule

Dong Yang,[†,‡] Jake L. Greenfield,[†] Tanya K. Ronson,[†] Larissa K. S. von Krbek,[†,×] Le Yu,[‡] Jonathan R. Nitschke[†]*

[†] Department of Chemistry, University of Cambridge, Lensfield Road, Cambridge, CB2 1EW, United Kingdom

[‡] Key Laboratory of Synthetic and Natural Functional Molecule of the Ministry of Education, College of Chemistry and Materials Science, Northwest University, Xi'an 710069, China

[×] Present Address: Kekulé-Institut für Organische Chemie und Biochemie der Rheinischen Friedrich-Wilhelms-Universität Bonn, Gerhard-Domagk-Str. 1, 53121 Bonn, Germany

---

Table of Contents:

S1. General considerations

The 2-methyl-quinolin-8-ylamine, 2,5-dibromopyridine (Acros Organics) and benzyl azide (Alfa Aesar) were purchased from Acros Organics and Alfa Aesar and used as received. All solvents and other reagents were of reagent grade quality and purchased commercially. ^{1}H and ^{13}C spectra were recorded on a Bruker Avance III-400 MHz spectrometer at 400 and 100 MHz, respectively, using the residual solvent peak as an internal standard for ^{1}H and ^{13}C. ^{1}H-^{13}C HSQC, ^{1}H-^{1}H COSY and ^{1}H-^{1}H NOESY spectra were recorded on a Bruker Avance III-500 MHz TCI cryoprobe spectrometer. ^{19}F NMR spectra were recorded on a Bruker Avance III-500 MHz HD Smart Probe Spectrometer.

UV-Vis measurements were performed on a Cary 100 UV-Vis spectrophotometer with a 1 cm path length cuvette at 298 K. Fluorescence measurements were performed on a Cary Eclipse fluorescence spectrophotometer at 298 K.

Low resolution electrospray ionisation mass spectrometry (ESI-MS) was undertaken on a Micromass Quattro LC mass spectrometer (cone voltage 5-30 eV; desolvation temperature 313 K; ionisation temperature 313 K) infused from a Harvard syringe pump at a rate of 10 μl·min^{-1}.

S2. Synthesis and characterization

2.1 Synthesis of subcomponent A

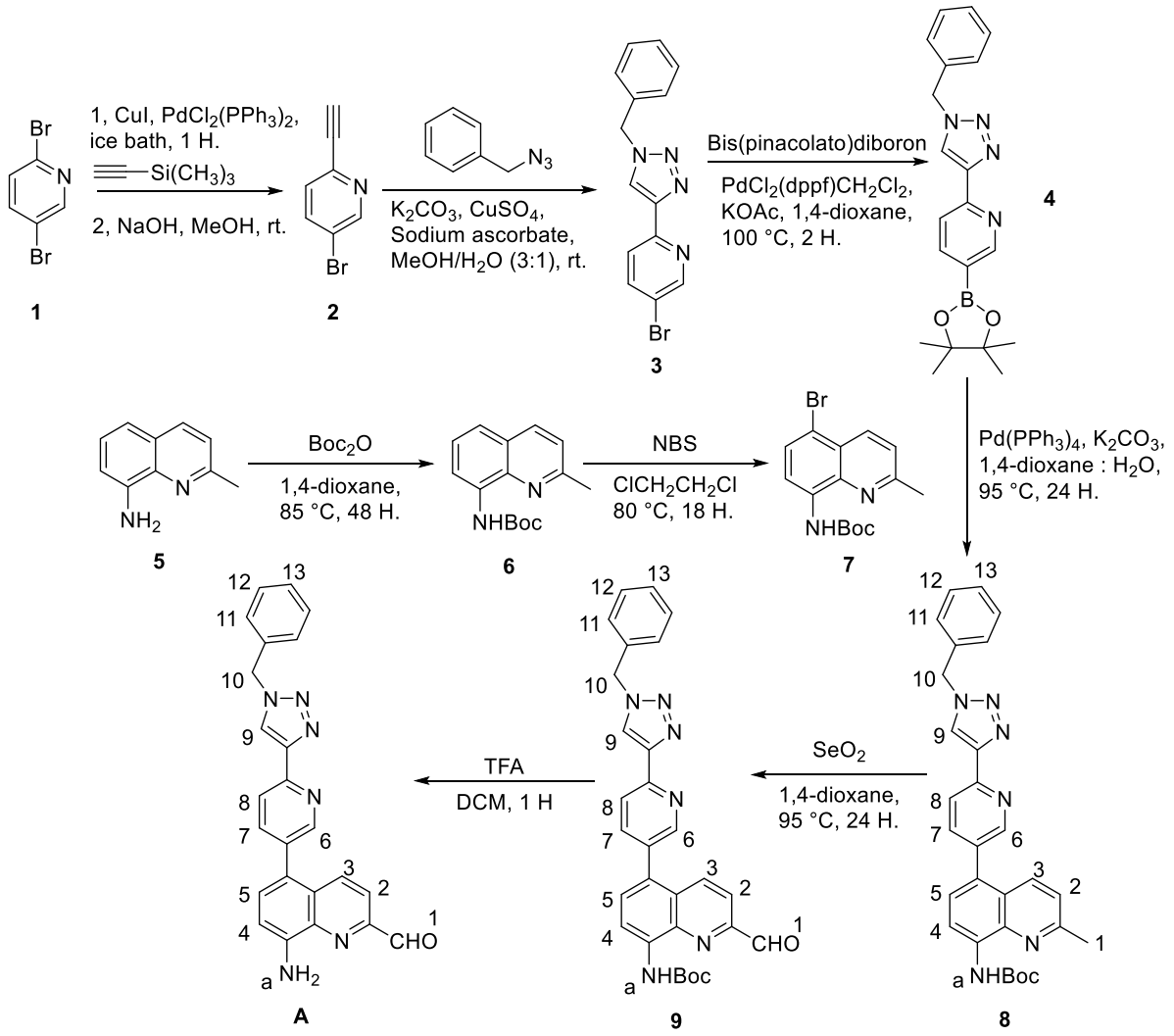

Scheme S1. Synthetic route for the preparation of subcomponent **A**. The NMR numbering scheme for **8**, **9** and **A** is shown.

Compound 2

Compound **2** was synthesized according to literature procedures.[1]

^{1}H NMR (400 MHz, $CDCl_3$, ppm): δ 8.651 (d, J = 4 Hz, 1 H) 7.790 (dd, J = 8 Hz, J = 4 Hz, 1 H), 7.362 (d, J = 8 Hz, 1 H), 3.216 (s, 1 H).

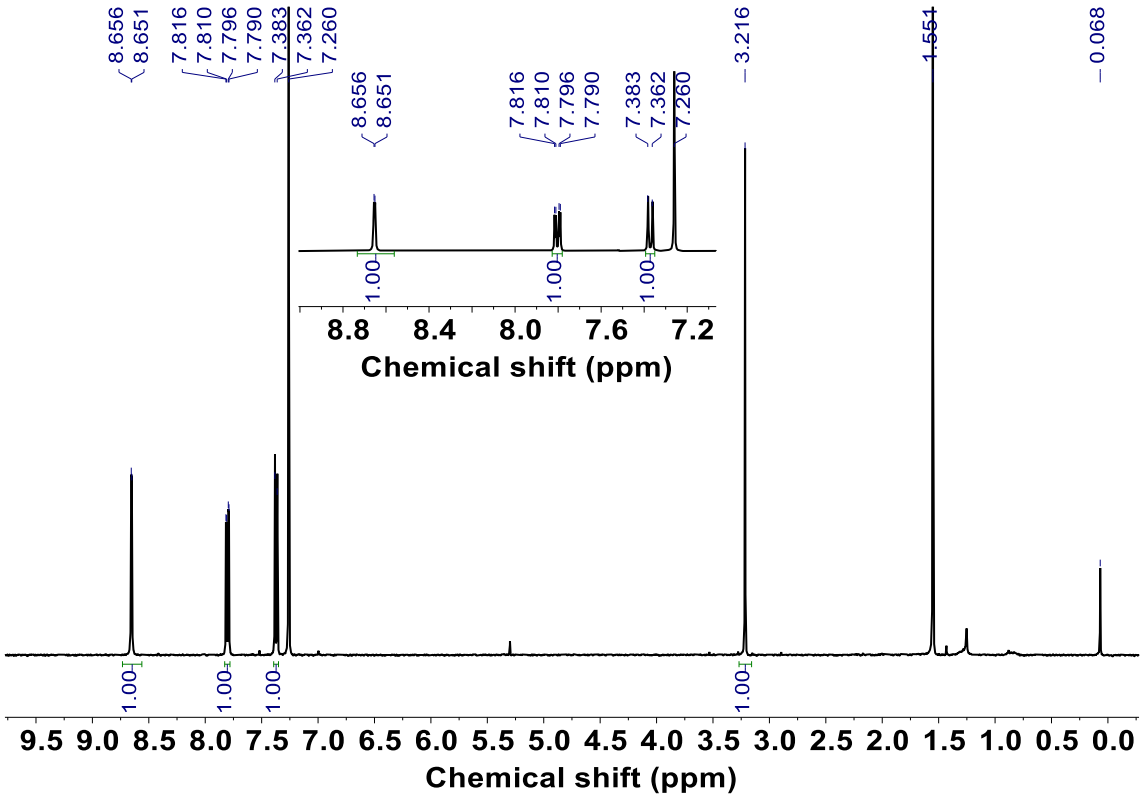

Figure S1. ^{1}H NMR spectrum ($CDCl_3$, 400 MHz, 298 K) of compound **2**.

Compound 3

Compound **2** (0.72 g, 3.4 mmol) and benzyl azide (0.5 mL, 4 mmol) were dissolved in a methanol/water mixture (3:1 ratio, 16 mL), using a round bottomed flask (50 mL). Then copper(II) sulfate (99.6 mg, 0.4mmol, dissolved in 4 mL water) and sodium ascorbate (364.5 mg, 1.84 mmol, dissolved in 4 mL water) were added. The reaction mixture turned yellow after a while and was stirred for 72 h at 25 ℃. The yellow precipitate was filtered and washed with methanol. The crude product was then dissolved in 20 mL dichloromethane and 20 mL 0.25 M aqueous EDTA solution was added to remove residual metal ions. The dichloromethane phase was collected and the solvent was removed by rotary evaporator and dried under vacuum to give compound **3** (1.0 g, 3.2 mmol, 95% yield). ^{1}H NMR (400 MHz, $CDCl_3$, ppm): δ 8.581 (s, 1H), 8.068 (d, J = 8.4 Hz, 1H), 8.020 (s, 1H), 7.874 (dd, J = 8.4 Hz, J = 2.4 Hz, 1H), 7.323-7.396 (m, 5H), 5.583 (s, 1H).

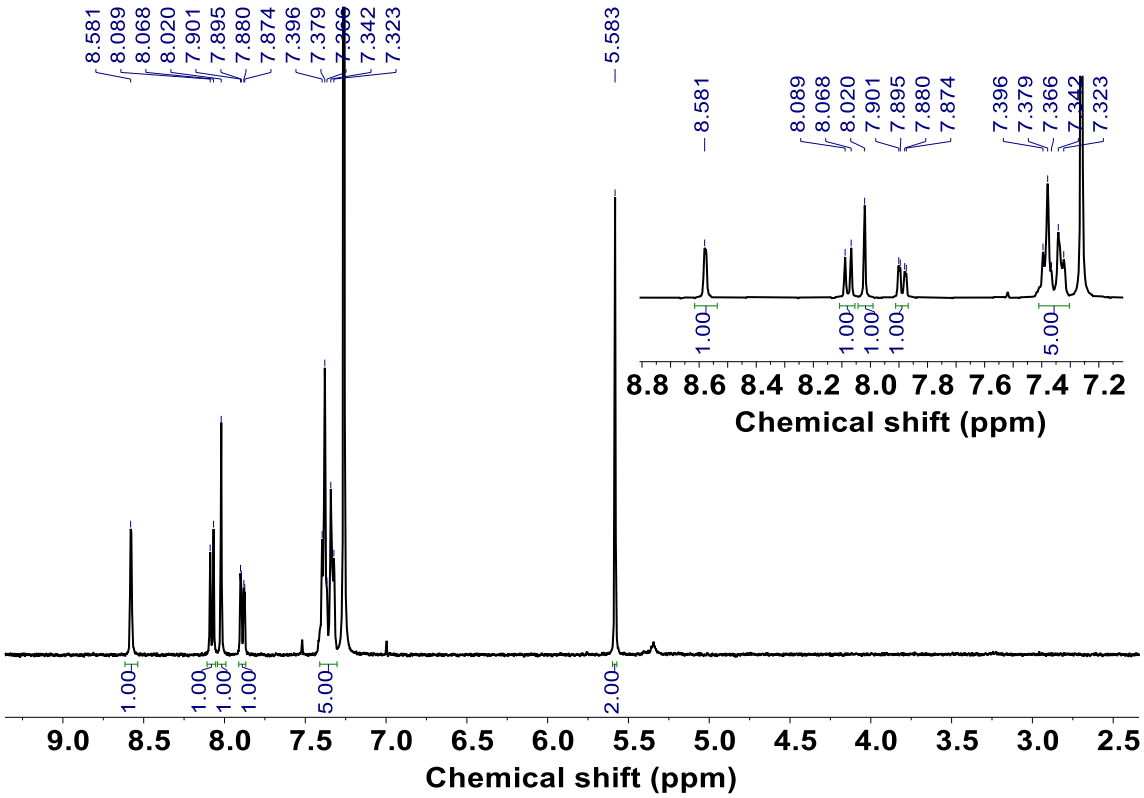

Figure S2. ^{1}H NMR spectrum ($CDCl_3$, 400 MHz, 298 K) of compound **3**.

Compound 6[2]

Compound **5** (1.58 g, 10 mmol) and di-tert-butyl decarbonate (5.4 g, 25 mmol) was added to 20 mL 1,4-dioxane and the reaction mixture was heated at 85 °C for 2 days. After completion of the reaction, the solvent was removed via rotary evaporator. The crude product was purified by silica gel column chromatography using DCM/hexane (1:1) as eluent to yield compound **6** (2.11 g, 82% yield) as white solid. ^{1}H NMR (400 MHz, $CDCl_3$, ppm): δ 9.052 (s, 1H), 8.363 (d, J = 7.6 Hz, 1H), 7.998 (d, J = 8.4 Hz, 1H), 7.412 (t, J = 7.6 Hz, 1H), 7.356 (d, J = 8.4 Hz, 1H), 7.285 (d, J = 8.4 Hz, 1H), 2.740 (s, 3H), 1.593 (s, 9H).

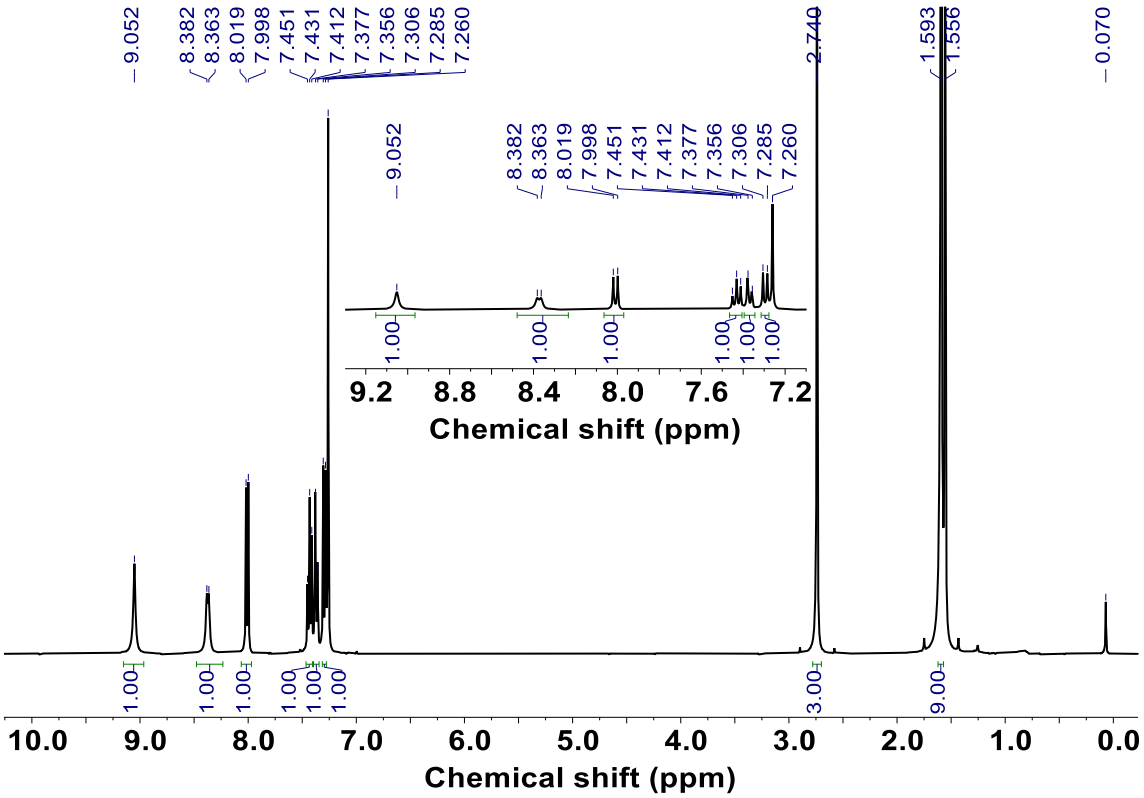

Figure S3. ^{1}H NMR spectrum ($CDCl_3$, 400 MHz, 298 K) of compound **6**.

Compound 7

Compound **7** was synthesized according to the literature procedures.[3] ^{1}H NMR (400 MHz, $CDCl_3$, ppm): δ 9.012 (s, 1H), 8.323 (d, J = 8.8 Hz, 1H), 8.248 (d, J = 8.4 Hz, 1H), 7.655 (d, J = 8.4 Hz, 1H), 7.357 (d, J = 8.8 Hz, 1H), 2.752 (s, 3H), 1.590 (s, 9H).

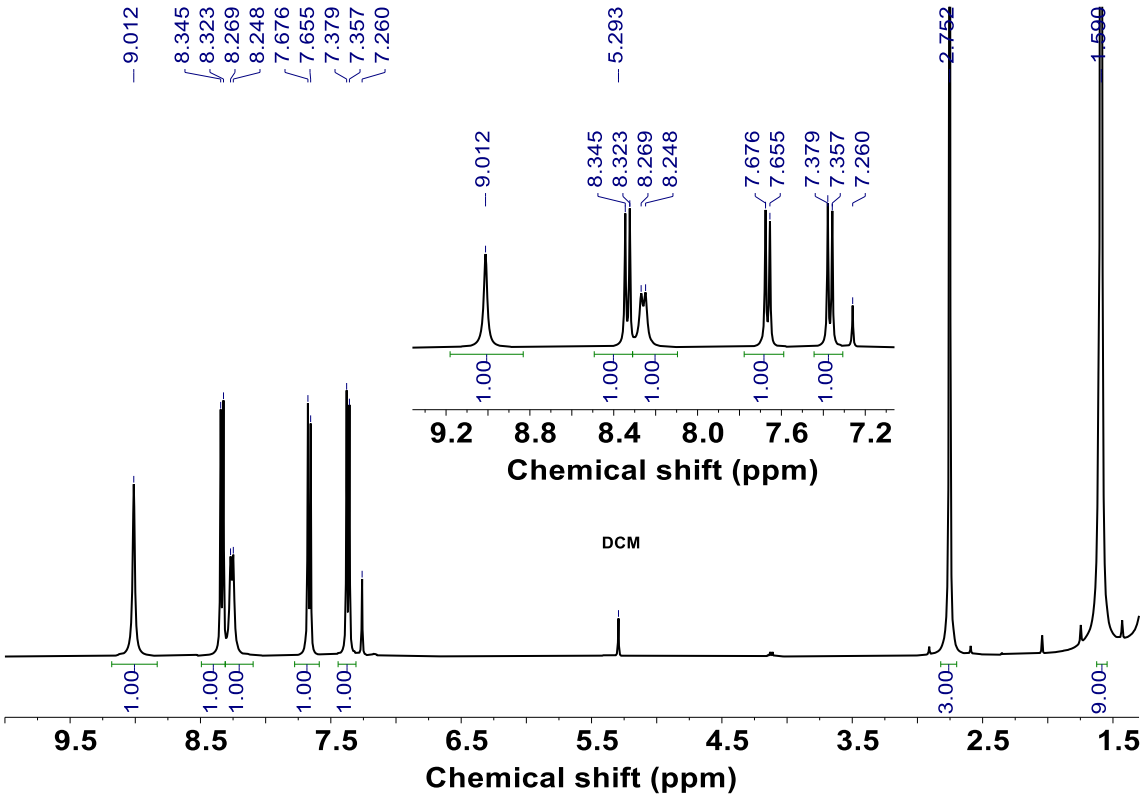

Figure S4. ^{1}H NMR spectrum ($CDCl_3$, 400 MHz, 298 K) of compound **7**.

Compound 8

A suspension of compound **3** (0.63 g, 2 mmol), bis(pinacolato)diboron (0.61 g, 2.4 mmol), $PdCl_2(dppf)CH_2Cl_2$ (81.6 mg, 0.1 mmol) and KOAc (0.39 g, 4 mmol) in 1,4-dioxane (5 mL) was degassed by bubbling with nitrogen for 10 mins. The suspension was heated under microwave conditions at 100 ℃ for 2 h. Then a black solution was obtained and transferred to a 50 mL three-necked flask. $Pd(PPh_3)_4$ (0.23 g, 0.2 mmol), K_2CO_3 (0.55 g, 4 mmol), compound **7** (0.67 g, 2 mmol) and a 1,4-dioxane/water mixture (4:1 ratio, 10 mL) were added to the solution. The solution was then degassed with nitrogen for 30 mins and heated at 95 ℃ for 24 h. After completion of the reaction, the solvent was removed via rotary evaporator. The crude product was purified by silica gel column chromatography using ethyl acetate/hexane (1:2) as eluent to yield compound **8** (0.39 g, 39% yield) as a white solid. ^{1}H NMR (400 MHz, $CDCl_3$, ppm): δ 9.159 (s, 1H, NHa), 8.615 (d, J = 2.0 Hz, 1H, H9), 8.446 (d, J = 8.0 Hz, 1H, H3), 8.287 (d, J = 8 Hz, 1H, H7), 8.098 (s, 1H, H6), 8.069 (d, J = 8.8 Hz, 1H, H5), 7.846 (dd, J = 8.4 Hz, J = 2.4 Hz, 1H, H8), 7.418 (d, J = 8.0 Hz, 1H, H4), 7.345-7.407 (m, 5H, H11-H13), 7.280 (d, J = 8.8 Hz, 1H, H2), 5.621 (s, 2H, H10), 2.757 (s, 3H, H1), 1.608 (s, 9H, NH*Boc*). ^{13}C NMR (100 MHz, $CDCl_3$, ppm): δ 157.3, 153.1, 150.3, 149.1, 148.7, 138.4, 137.8, 135.0, 134.6, 134.5, 134.0, 129.4, 129.1, 128.6, 128.5, 127.6, 124.5, 122.9, 122.1, 120.0, 114.1,

80.7, 54.6, 28.6, 25.2.

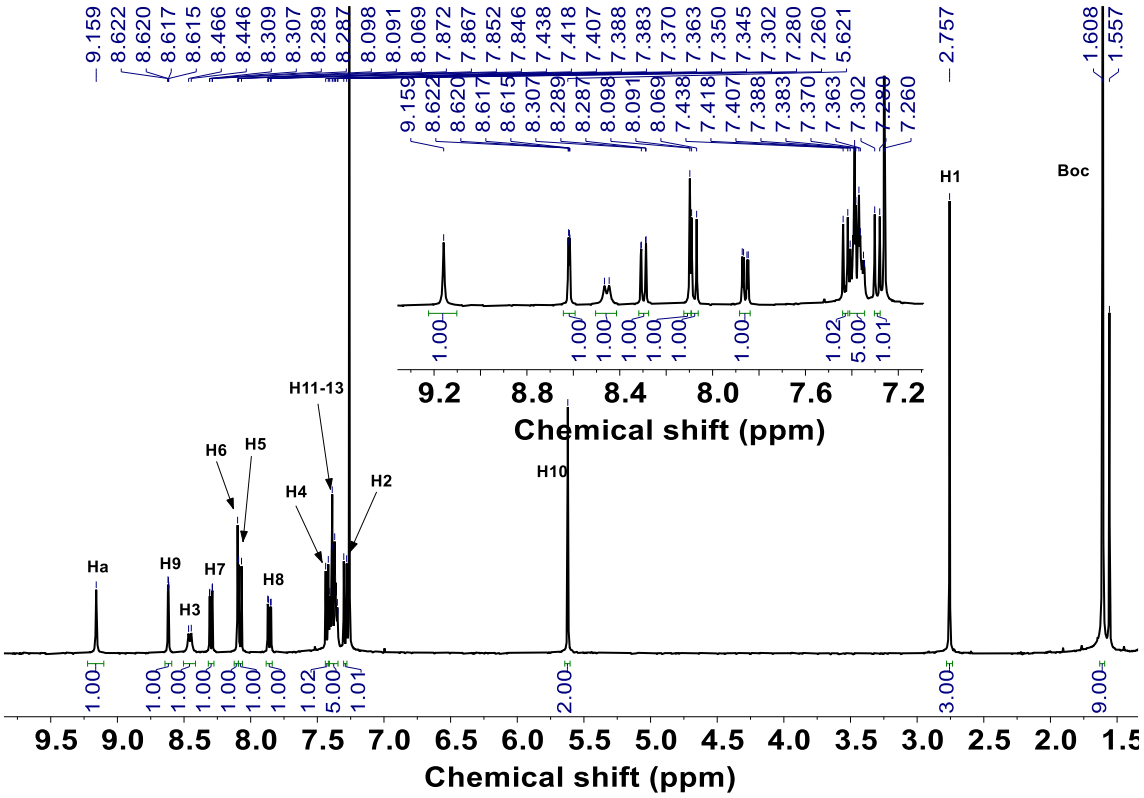

Figure S5. ^{1}H NMR spectrum ($CDCl_3$, 400 MHz, 298 K) of compound **8**.

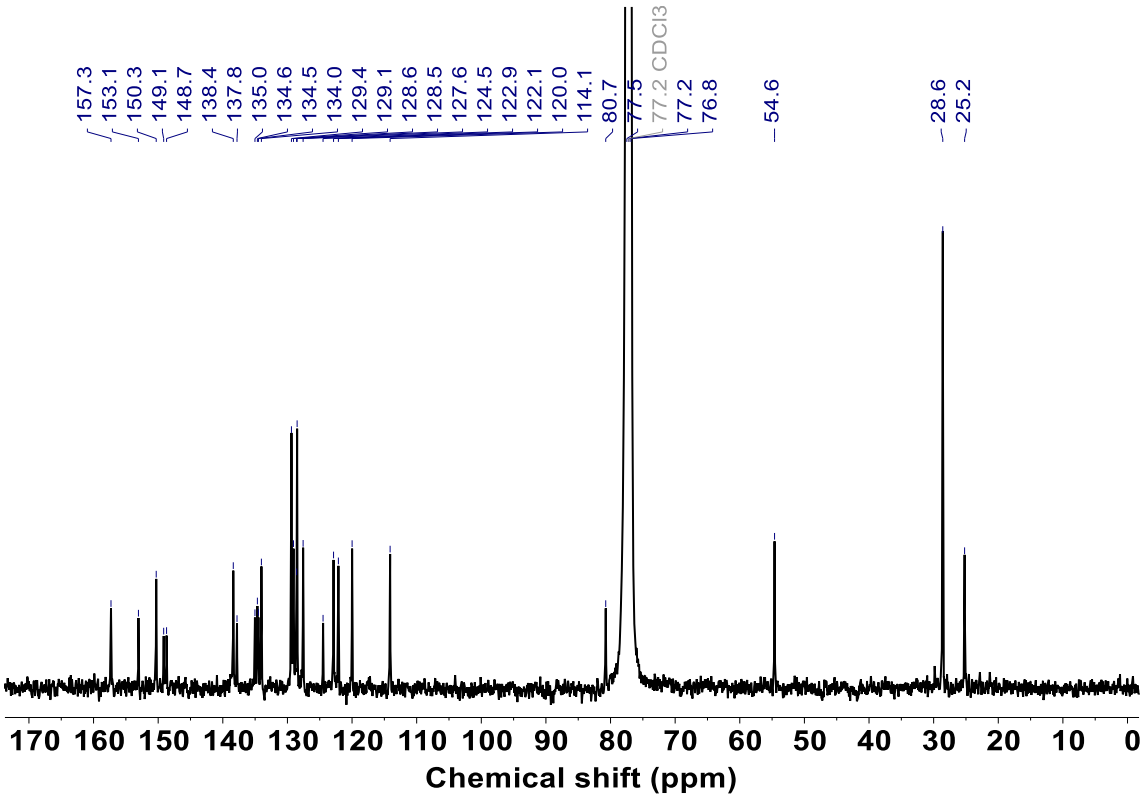

Figure S6. ^{13}C NMR spectrum ($CDCl_3$, 100 MHz, 298 K) of compound **8**.

Compound 9

Compound **8** (0.3 g, 0.61 mmol) was dissolved in dry dioxane (12 mL). SeO_2 (0.4 g, 3.66 mmol) was added to the mixture which was subsequently left to stir at 95 ℃ for 24 h. The reaction mixture was filtered and the filtrate was concentrated *in vacuo*. The crude product was purified by silica gel column chromatography using ethyl acetate/hexane (1:2) as eluent to yield compound **9** (0.2 g, 65% yield) as a white solid. ^{1}H NMR (400 MHz, $CDCl_3$, ppm): δ 10.287 (s, 1H, H1), 9.099 (s, 1H, NHa), 8.619 (d, J = 2.4 Hz, 1H, H9), 8.601 (d, J = 7.2 Hz, 1H, H3), 8.357 (d, J = 8.8 Hz, 1H, H4), 8.328 (d, J = 7.2 Hz, 1H, H7), 8.112 (s, 1H, H6), 8.024 (d, J = 8.8 Hz, 1H, H5), 7.859 (dd, J = 8.0 Hz, J = 2.4 Hz, 1H, H8), 7.647 (d, J = 8.0 Hz, 1H, H2), 7.350-7.433 (m, 5H, H11-H13), 5.627 (s, 2H, H10), 1.629 (s, 9H, NH*Boc*). ^{13}C NMR (100 MHz, $CDCl_3$, ppm): δ 193.0, 152.8, 150.3, 150.2, 149.7, 148.5, 138.4, 137.9, 136.5, 135.5, 134.4, 133.8, 131.5, 129.4, 129.1, 128.9, 128.5, 128.4, 122.3, 120.2, 118.1, 115.1, 81.5, 54.6, 28.5. HR-MS *m/z*: found 507.2145, calcd for $C_{29}H_{27}N_6O_3$ $[M+H]^+$ 507.2139.

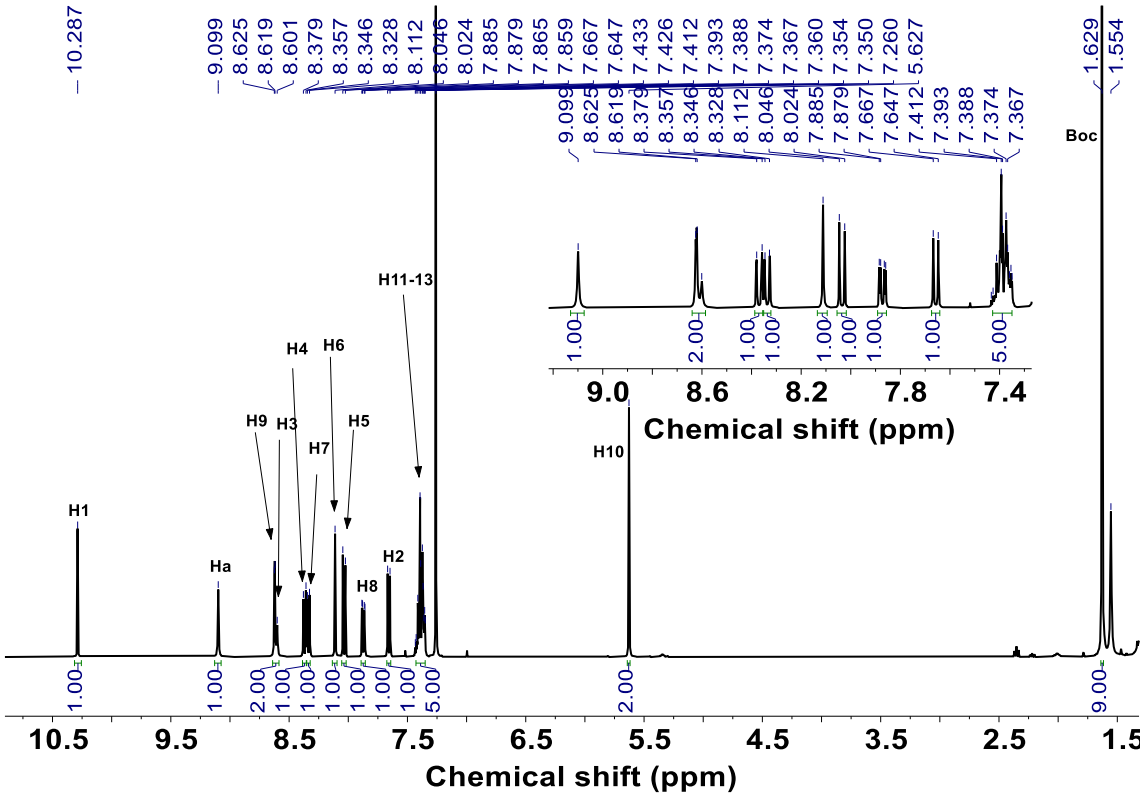

Figure S7. ^{1}H NMR spectrum ($CDCl_3$, 400 MHz, 298 K) of compound **9**.

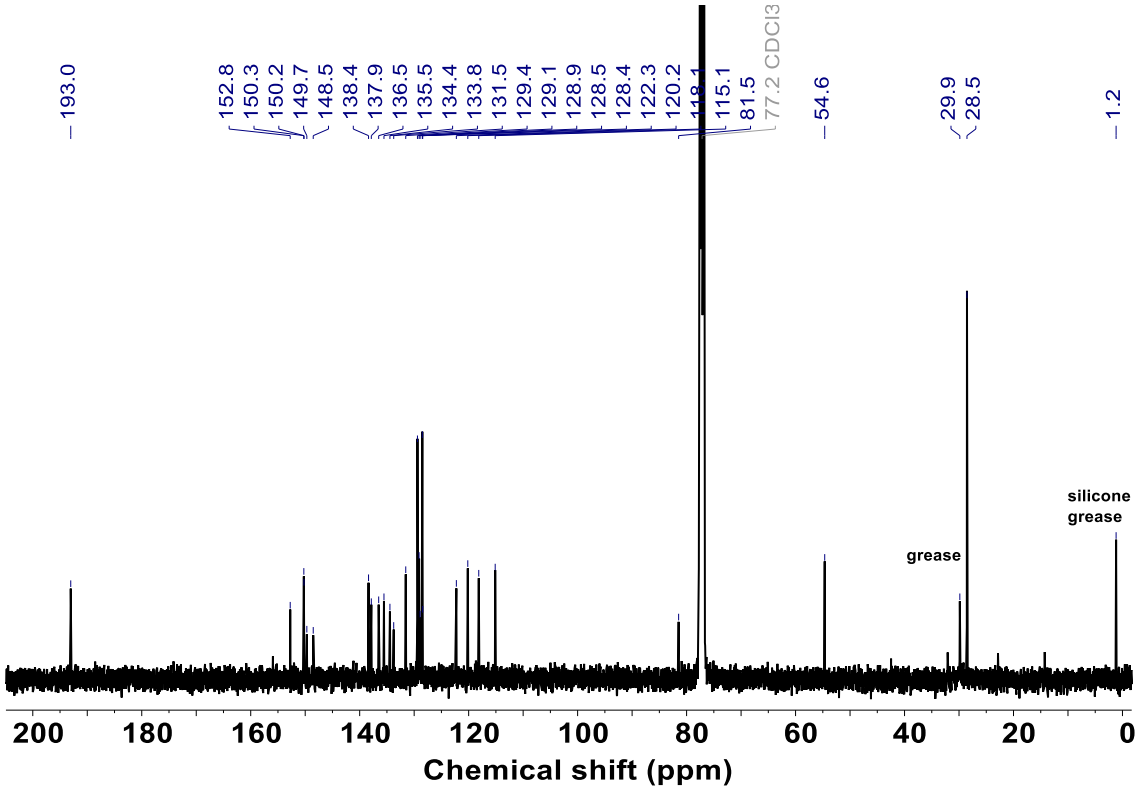

Figure S8. ^{13}C NMR spectrum ($CDCl_3$, 100 MHz, 298 K) of compound **9**.

Subcomponent A

Compound **9** (0.2 g, 0.4 mmol) was dissolved in a mixture of dichloromethane and trifluoroacetic acid (3:1 *v/v*, 24 mL) and stirred at room temperature for 1 h. The dark red solution was then poured over ice and brought to pH 7 by the addition of sodium bicarbonate. The organic phase was extracted with dichloromethane, washed with brine (3 × 50 mL), dried over $MgSO_4$ and finally concentrated *in vacuo*. The product was isolated as a dark orange crystalline solid, **A** (0.13 g, 80 % yield). ^1H NMR (400 MHz, $CDCl_3$, ppm): δ 10.205 (s, 1H, H1), 8.614 (s, 1H, H9), 8.296 (d, J = 8.0 Hz, 1H, H3), 8.288 (d, J = 8.4 Hz, 1H, H7), 8.098 (s, 1H, H6), 7.959 (d, J = 8.8 Hz, 1H, H4), 7.840 (d, J = 8.4 Hz, 1H, H8), 7.467 (d, J = 8.0 Hz, 1H, H5), 7.371-7.409 (m, 5H, H11-H13), 7.055 (d, J = 7.6 Hz, 1H, H2), 5.623 (s, 2H, H10), 5.358 (s, 2H, NHa). ^{13}C NMR (100 MHz, $CDCl_3$, ppm): δ 193.4, 150.3, 149.9, 149.1, 148.7, 145.5, 138.3, 137.7, 134.8, 134.5, 131.9, 129.4, 129.1, 129.0, 128.5, 124.3, 122.1, 120.1, 118.0, 110.1, 54.6. HR-MS *m/z*: found 407.1620, calcd for $C_{24}H_{19}N_6O$ $[M+H]^+$ 407.1615

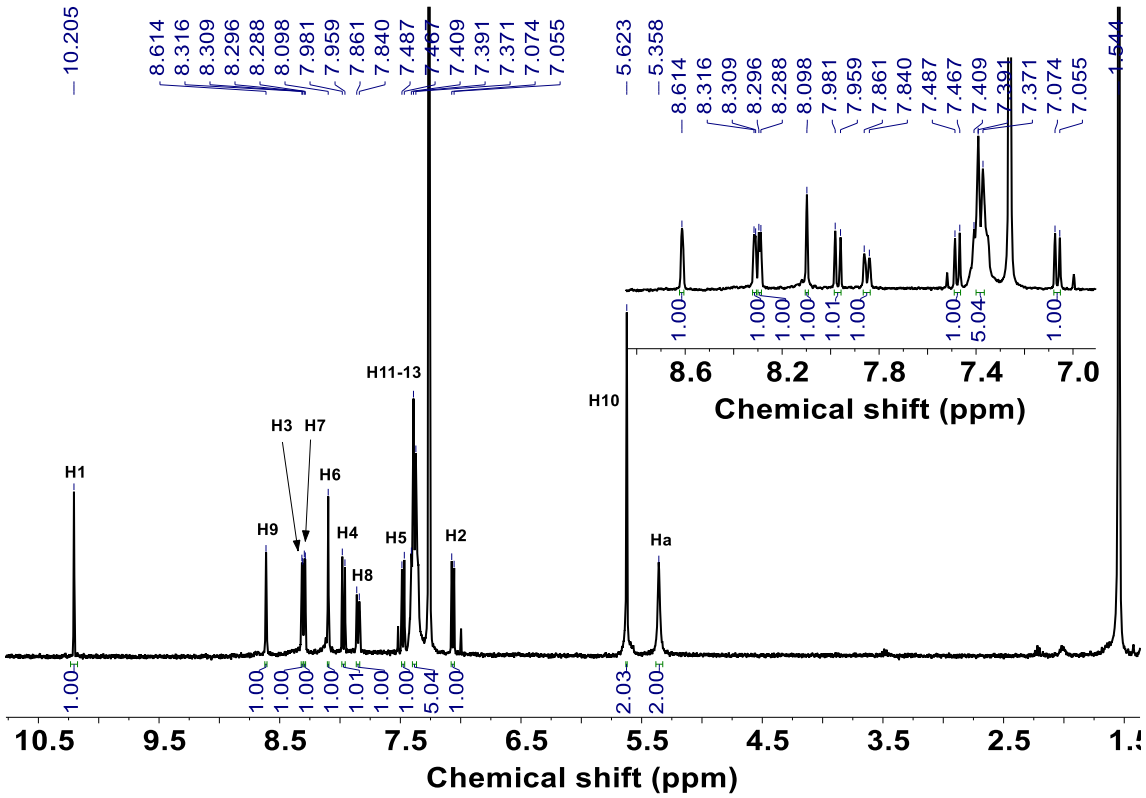

Figure S9. ^{1}H NMR spectrum ($CDCl_3$, 400 MHz, 298 K) of subcomponent **A**.

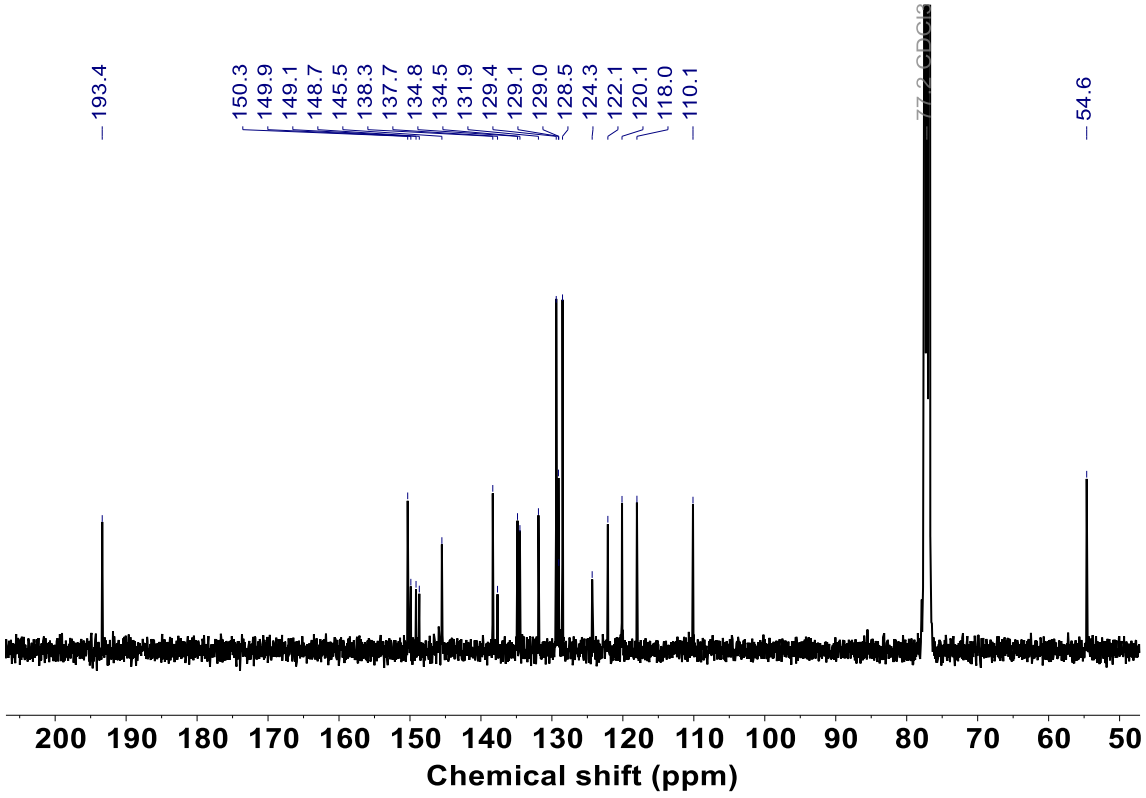

Figure S10. ^{13}C NMR spectrum ($CDCl_3$, 100 MHz, 298 K) of subcomponent **A**.

2.2 Preparation of tetrahedral capsule 1

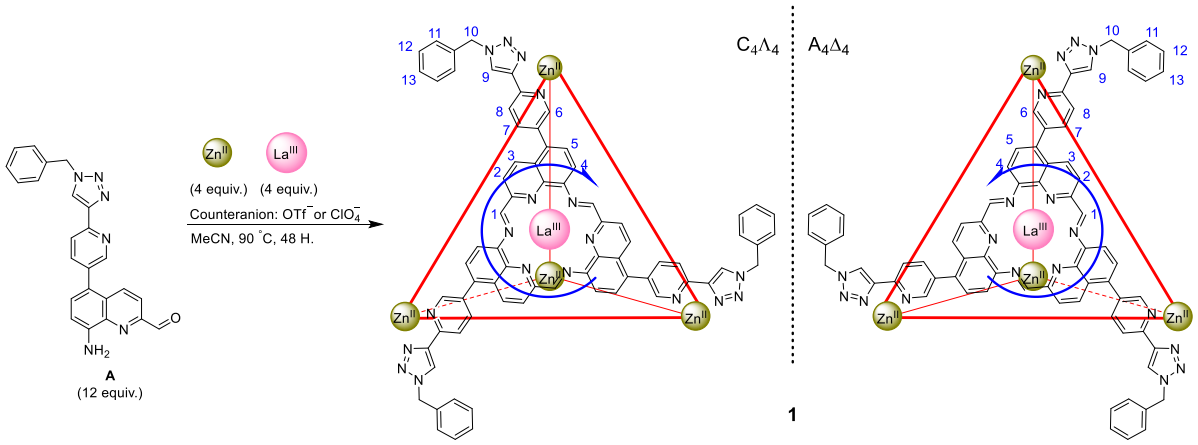

Scheme S2. Subcomponent self-assembly of Zn^{II}–La^{III} heterobimetallic **1**.

1·(OTf)$_{20}$

Subcomponent **A** (2.44 mg, 6 μmol) was added to acetonitrile (5 mL) together with La(OTf)$_3$ (1.20 mg, 2.2 μmol) and Zn(OTf)$_2$ (0.82 mg, 2.2 μmol). The reaction was kept at 90 ℃ for 24 h. Centrifugation was used to remove the precipitate from the solution. Diethyl ether (Et_2O) (15 mL) was added to the solution. The orange powder was collected by centrifugation and dried under reduced pressure (3 mg, 80% yield). ^{1}H NMR (500 MHz, CD_3CN, ppm): δ 9.22 (s, 12H, H1); 8.90 (s, 12H, H9); 8.70 (d, J =10.0 Hz, 12H, H3); 8.49 (d, J = 10.0 Hz, 12H, H2), 8.40 (s, 12H, H7) 8.35-8.42 (m, 12H, H6/H8/H4), 7.70 (d, J = 10 Hz, 12H, H5); 7.40-7.48 (m, 60H, H11-H13); 5.74 (s, 24H, H10).

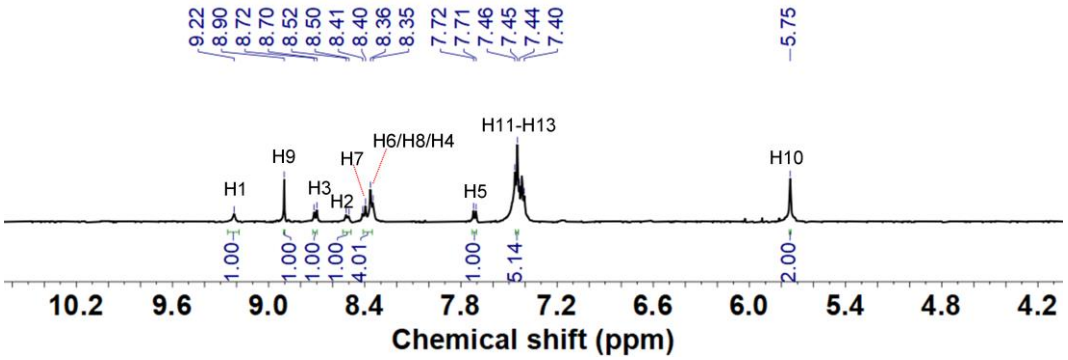

Figure S11. ^{1}H NMR spectrum (CD_3CN, 500 MHz, 298 K) of **1**·(OTf)$_{20}$.

1·(ClO$_4$)$_{20}$

Subcomponent **A** (30 mg, 73.9 μmol) was added to acetonitrile (20 mL) together with La(ClO$_4$)$_3$·6H_2O (14.59 mg, 26.7 μmol) and Zn(ClO$_4$)$_2$·6H_2O (9.94 mg, 26.7 μmol). The reaction was kept at 90 ℃ for 24 h. Centrifugation was used to remove the precipitate from the solution. Diethyl ether (Et_2O) (15 mL) was added

to the solution. The orange powder was collected by centrifugation and dried under reduced pressure (39 mg, 85% yield). ^{1}H NMR (500 MHz, CD_3CN, ppm): δ 9.21 (s, 12H, H1); 8.89 (s, 12H, H9); 8.74 (d, J =10.0 Hz, 12H, H3); 8.57 (d, J = 10.0 Hz, 12H, H2), 8.45 (d, J = 10.0 Hz, 12H, H4) 8.43 (d, J = 10.0 Hz, 12H, H7), 8.41(s, 12H, H6); 8.35 (d, J = 10.0 Hz, 12H, H8); 7.72 (d, J = 10 Hz, 12H, H5); 7.43-7.53 (m, 60H, H11-H13); 5.75 (s, 24H, H10).

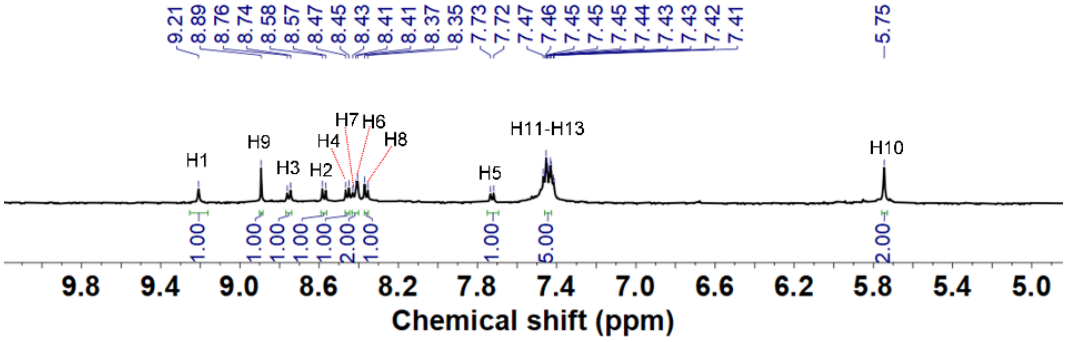

Figure S12. ^{1}H NMR spectrum (CD_3CN, 500 MHz, 298 K) of **1**·$(ClO_4)_{20}$.

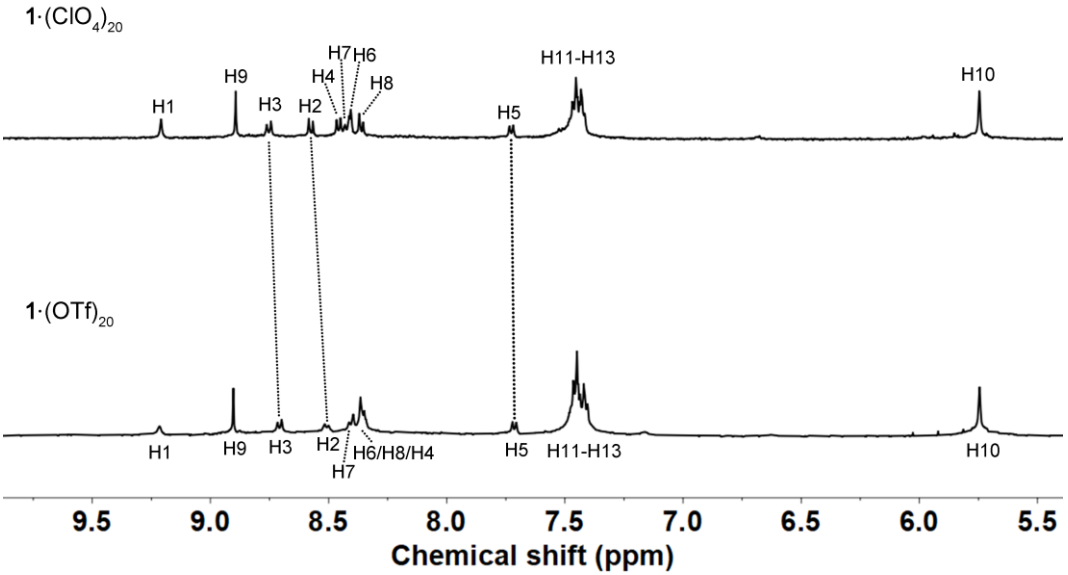

Figure S13. ^{1}H NMR spectra (CD_3CN, 500 MHz, 298 K) of **1**·$(ClO_4)_{20}$ and **1**·$(OTf)_{20}$.

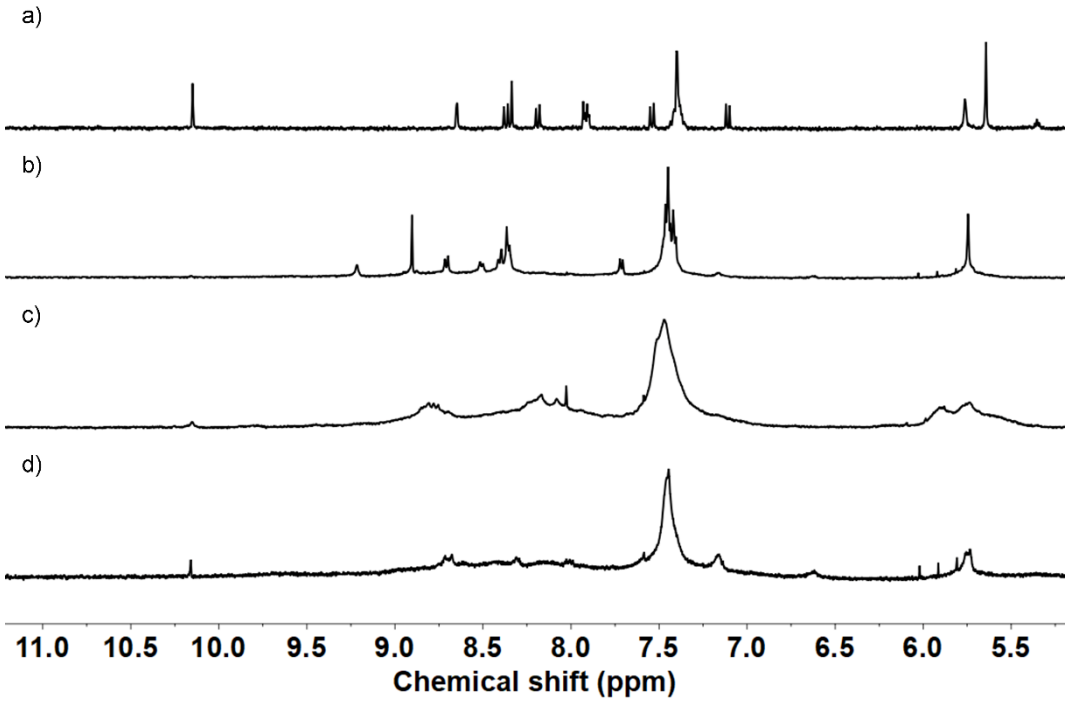

Figure S14. ^{1}H NMR spectra (CD_3CN, 500 MHz, 298 K) of a) subcomponent **A**; b) subcomponent **A** (12 equiv), $La(OTf)_3$ (4 equiv) and $Zn(OTf)_2$ (4 equiv); c) subcomponent **A** (12 equiv) and $Zn(OTf)_2$ (8 equiv); d) subcomponent **A** (12 equiv) and $La(OTf)_3$ (8 equiv).

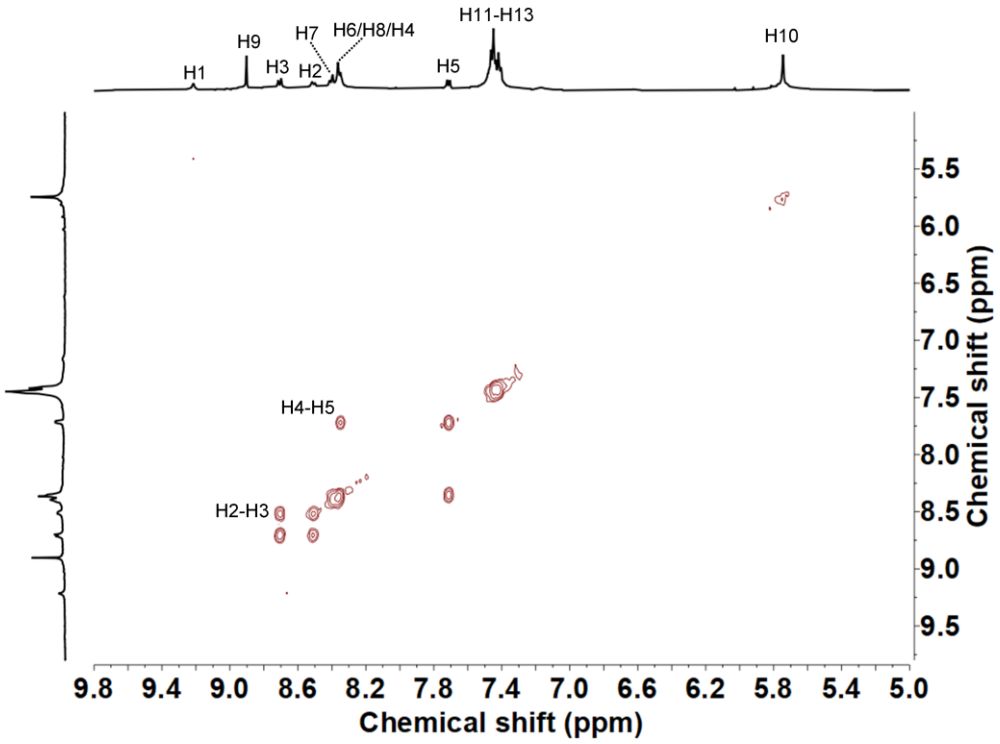

Figure S15. ^{1}H-^{1}H COSY (CD_3CN, 500 MHz, 298 K) of **1**·$(OTf)_{20}$.

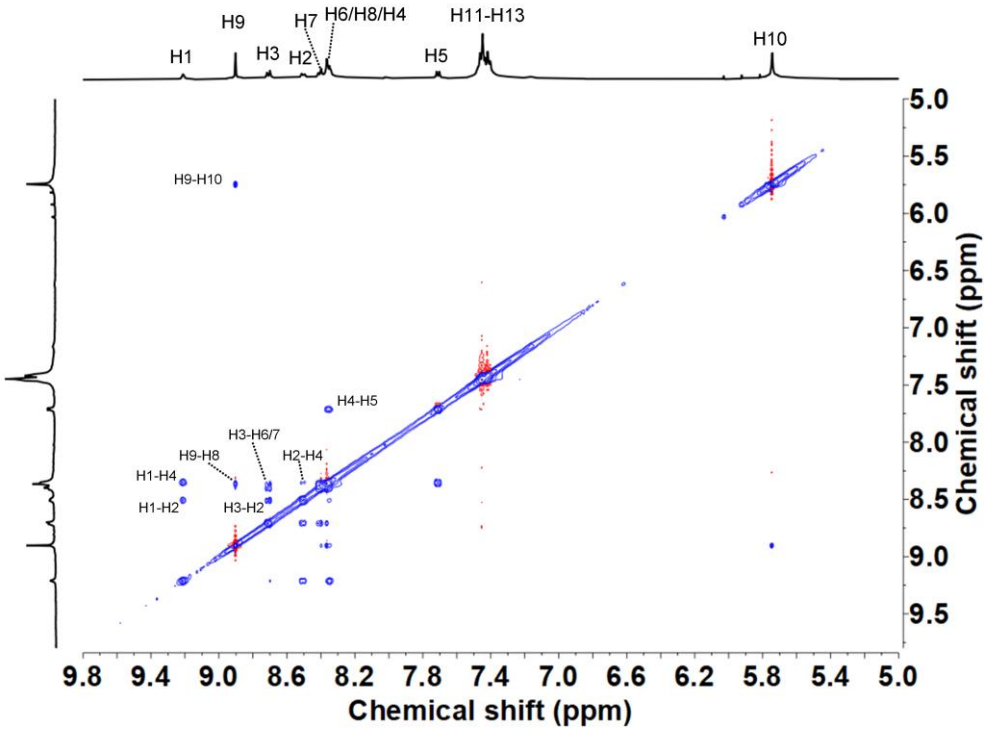

Figure S16. ^{1}H-^{1}H NOESY (CD_3CN, 500 MHz, 298 K) of **1**·$(OTf)_{20}$.

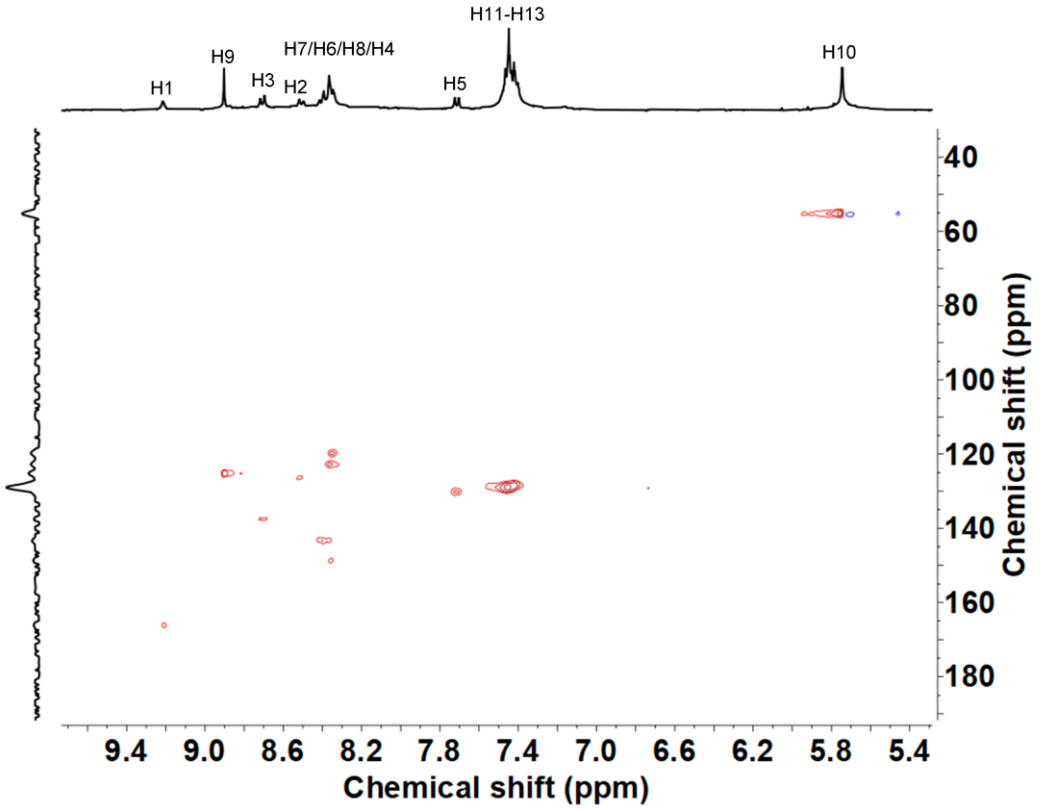

Figure S17. ^{1}H-^{13}C HSQC (CD_3CN, 400 MHz, 298 K) of **1**·$(OTf)_{20}$.

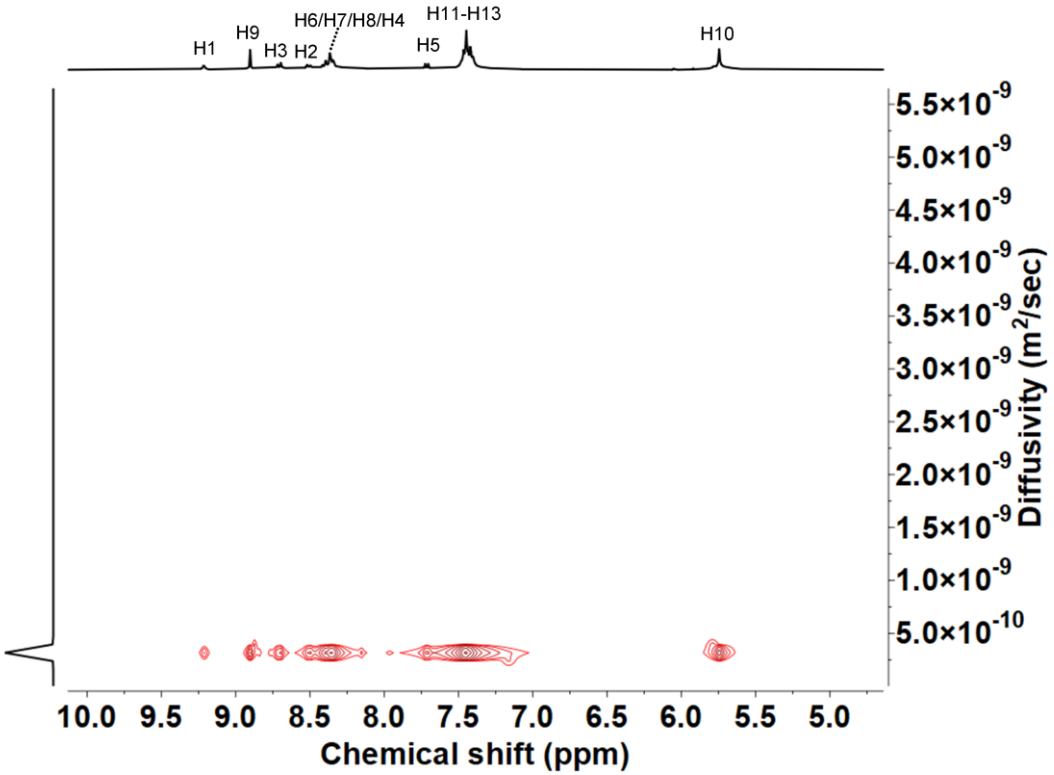

Figure S18. ^{1}H DOSY spectrum (CD_3CN, 400 MHz, 298 K) of **1**·$(OTf)_{20}$. The diffusion coefficient of **1**·$(OTf)_{20}$ in CD_3CN was measured to be 3.2 × 10^{-10} m^2 s^{-1}.

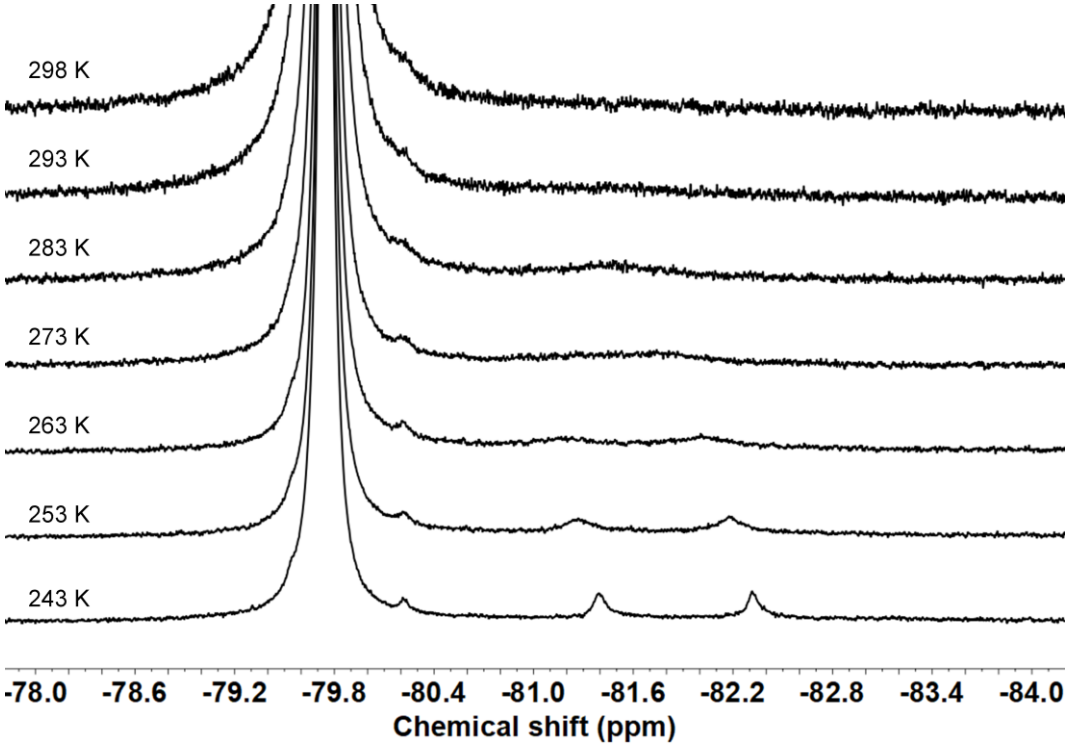

Figure S19. VT-^{19}F NMR spectra (CD_3CN, 470.4 MHz) of **1**·$(OTf)_{20}$.

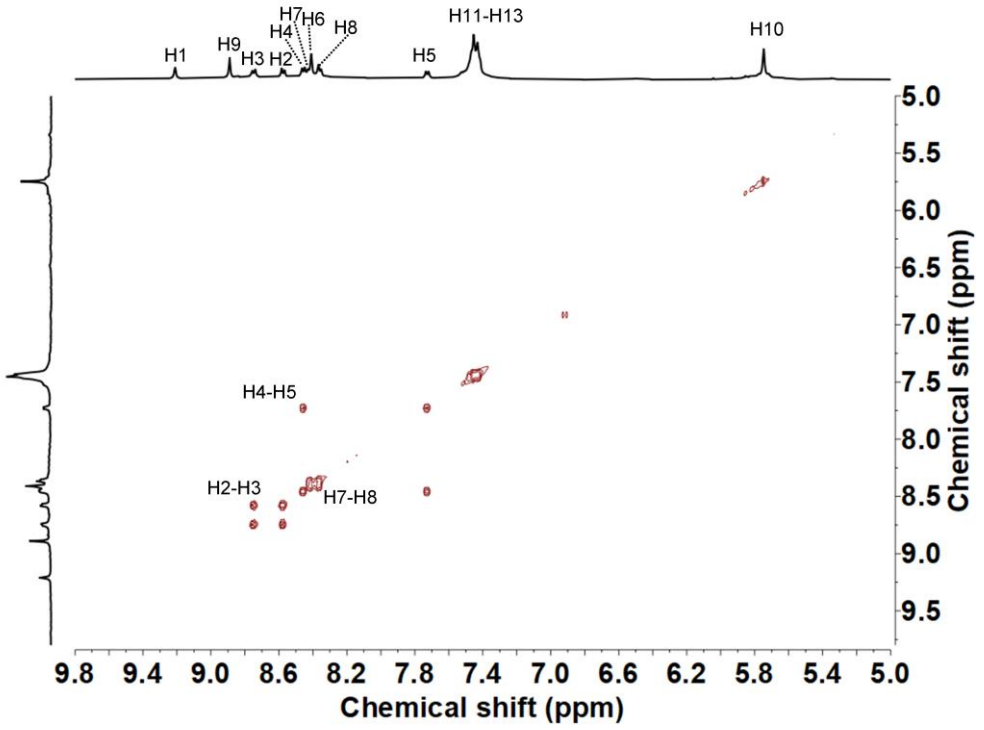

Figure S20. ^{1}H-^{1}H COSY (CD_3CN, 500 MHz, 298 K) of **1**·$(ClO_4)_{20}$

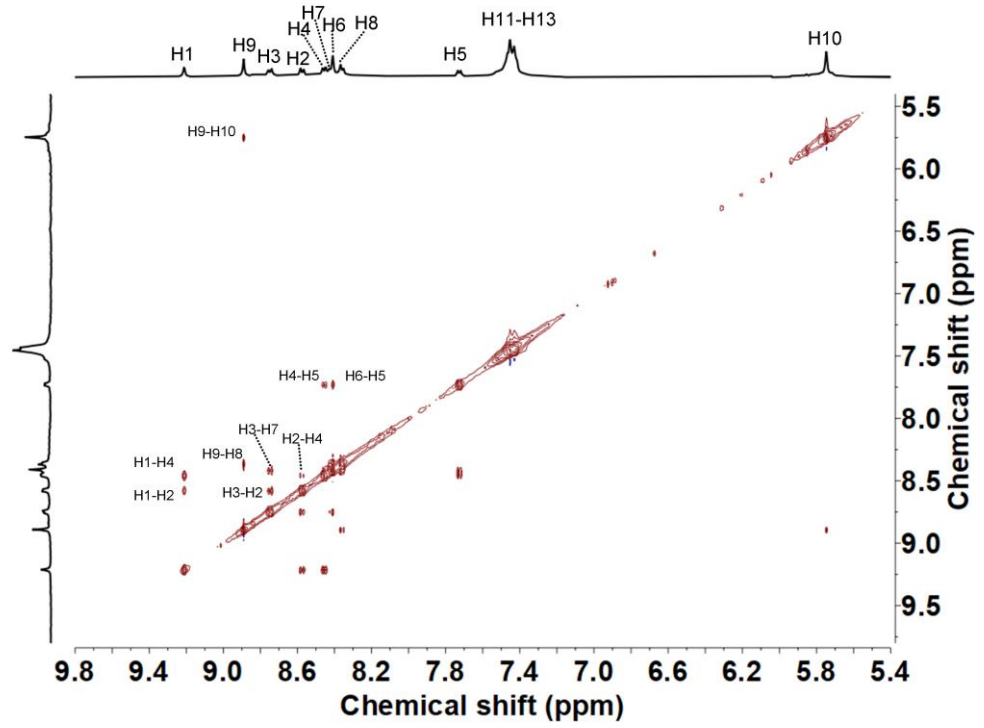

Figure S21. ^{1}H-^{1}H NOESY (CD_3CN, 500 MHz, 298 K) of **1**·$(ClO_4)_{20}$

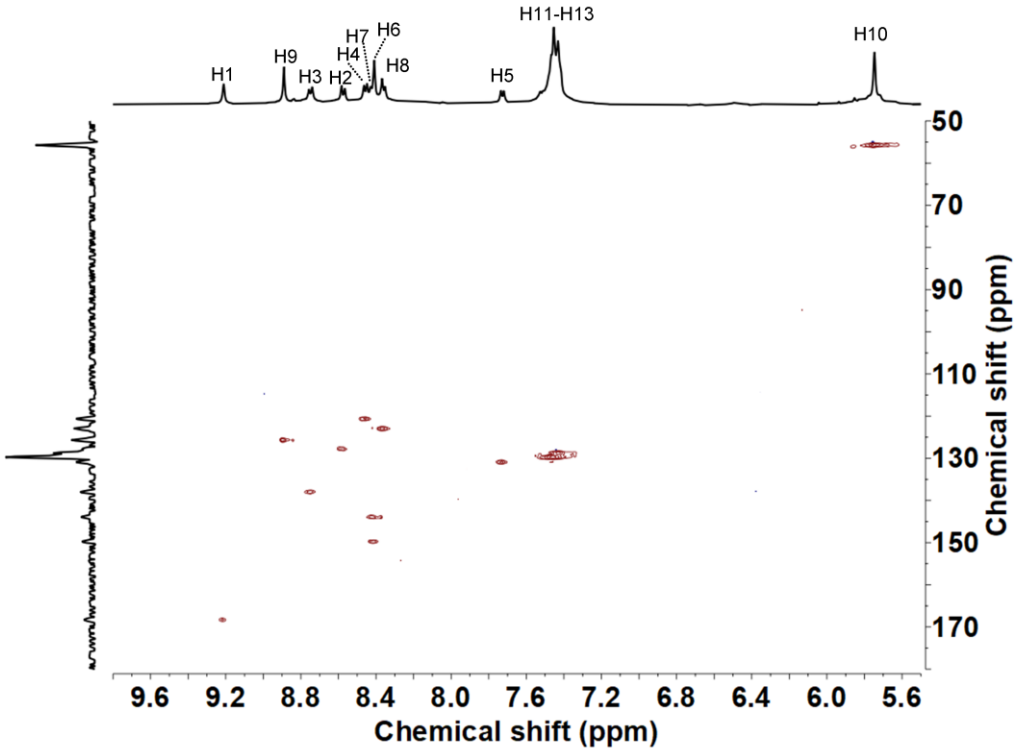

Figure S22. ^{1}H-^{13}C HSQC (CD_3CN, 500 MHz, 298 K) of **1**·$(ClO_4)_{20}$

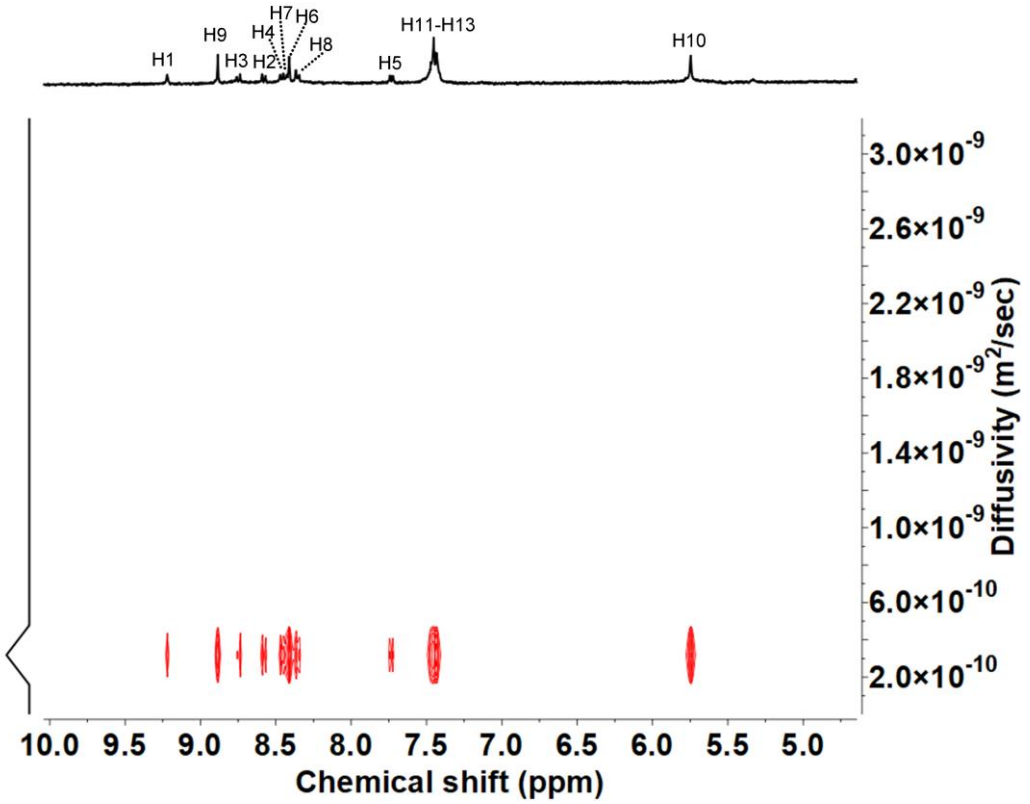

Figure S23. ^{1}H DOSY spectrum (CD_3CN, 400 MHz, 298 K) of **1**·$(ClO_4)_{20}$. The diffusion coefficient of **1**·$(OTf)_{20}$ in CD_3CN was measured to be 3.2×10^{-10} $m^2 \cdot s^{-1}$.

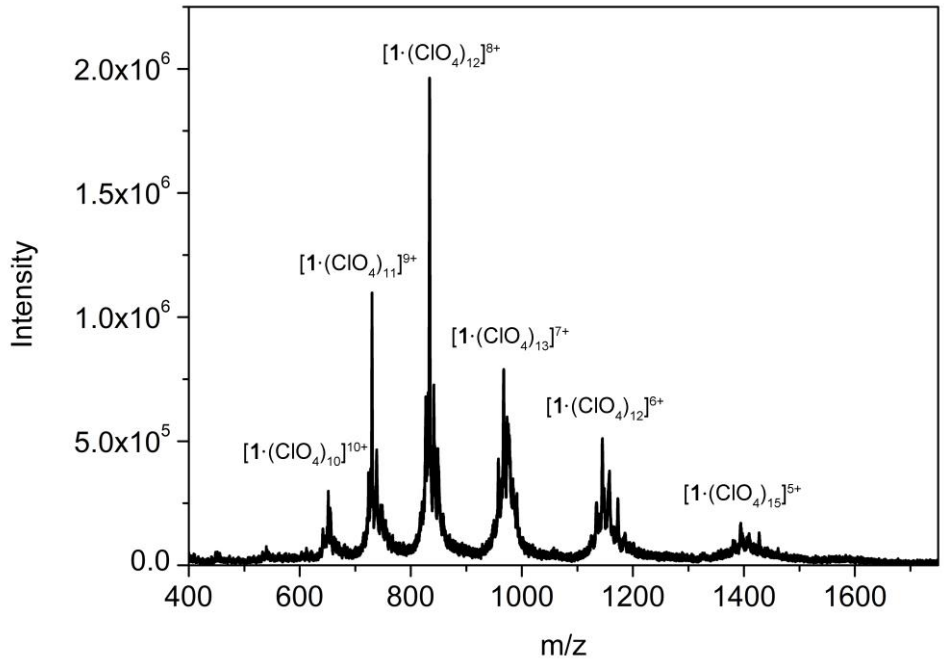

Figure S24. Low-resolution ESI-mass spectrometry analysis of **1**·$(ClO_4)_{20}$.

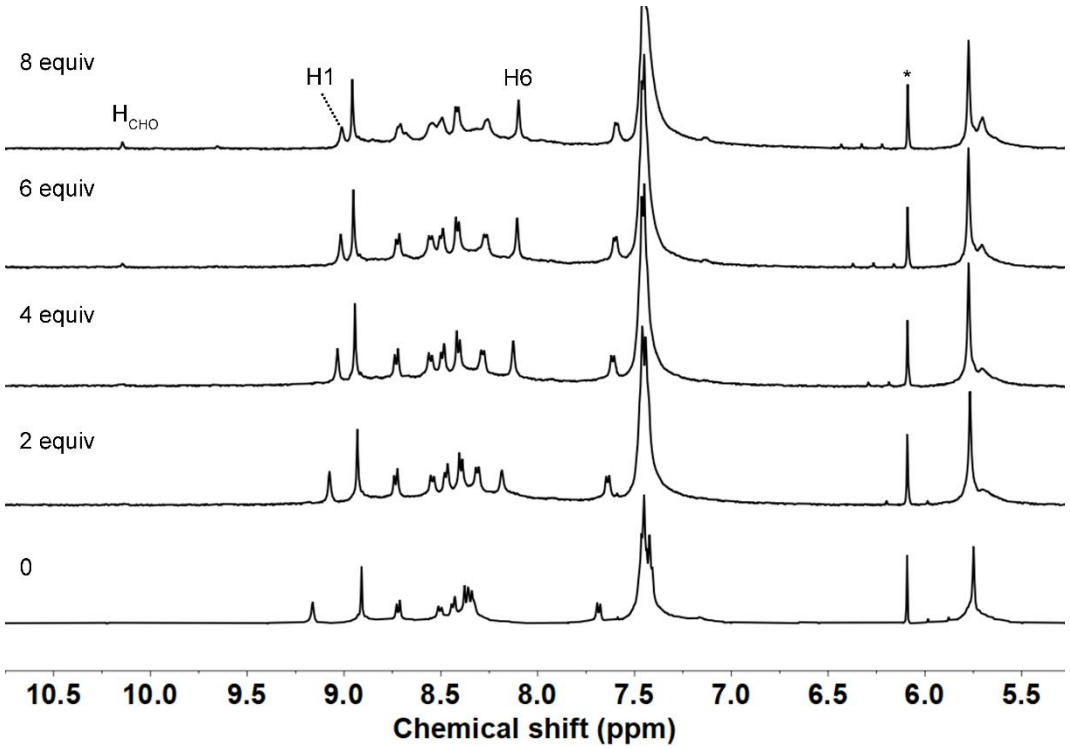

Figure S25. ^{1}H NMR spectra (CD_3CN, 500 MHz, 298 K) of subcomponent **A**, and **1**·$(OTf)_{20}$ (c = 62 μM) upon addition of 0 – 8 equiv. of Na_2EDTA. Guest equivalents with respect to the host are given on the left. The phenyl peak of the internal standard 1,3,5-trimethoxybenzene is indicated by an asterisk.

Attempts to construct of 1 using other counter anions

Several larger anions, such as tetrakis(3,5-bis(trifluoromethyl)phenyl)borate ($BArF^-$) and bis(trifluoromethanesulfon)imide (Tf_2N^-), were employed as counter ions in order to prepare an 'empty' capsule. Only broad signals were observed in the ^1H NMR spectra, however. In the case of Tf_2N^-, the spectrum of **1**·$(NTf_2)_{20}$ sharpened when TfO^- was added. We infer that anions such as TfO^- act as templates during the formation of capsule **1**.

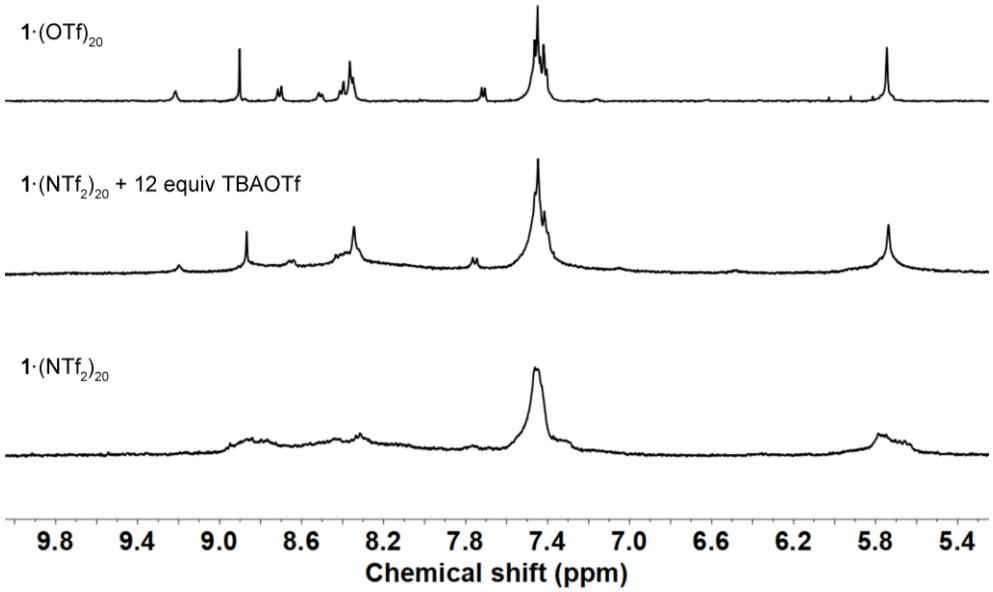

Figure S26. ^1H NMR spectra (CD_3CN, 400 MHz, 298 K) of **1**·$(NTf_2)_{20}$ (0.5 mM), **1**·$(NTf_2)_{20}$ with addition of 12 equiv of TBAOTf and **1**·$(OTf)_{20}$.

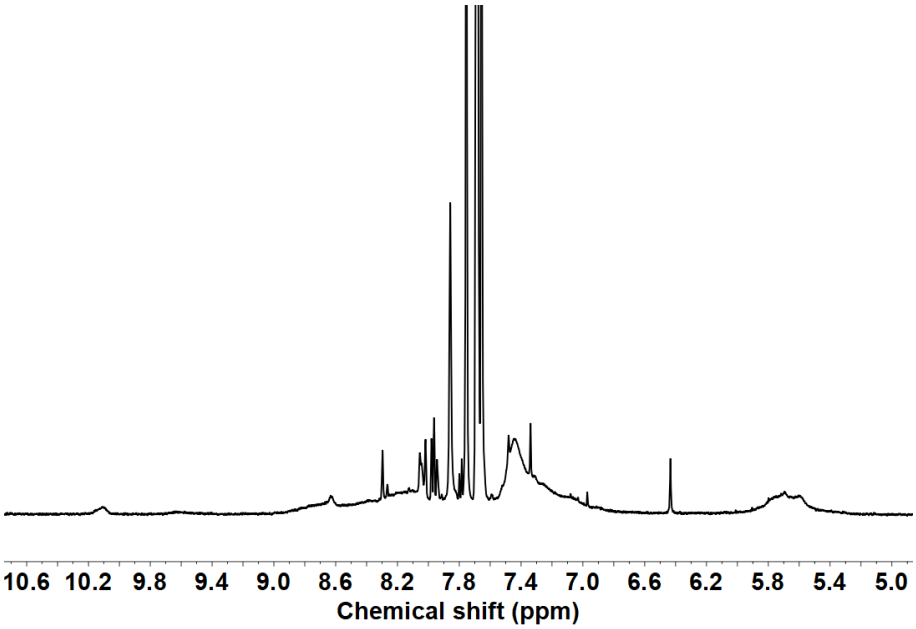

Figure S27. ^1H NMR spectra (CD_3CN, 500 MHz, 298 K) of subcomponent **A** (12 equiv), $La(BArF^-)_3$ (4 equiv) and $Zn(BArF^-)_2$ (4 equiv),[4] where $BArF^-$ is tetrakis(3,5-bis(trifluoromethyl)phenyl)borate.

S3. Host-guest chemistry of 1

S3.1 Characterisation data for host-guest complexes

S3.1.1 ^{1}H NMR

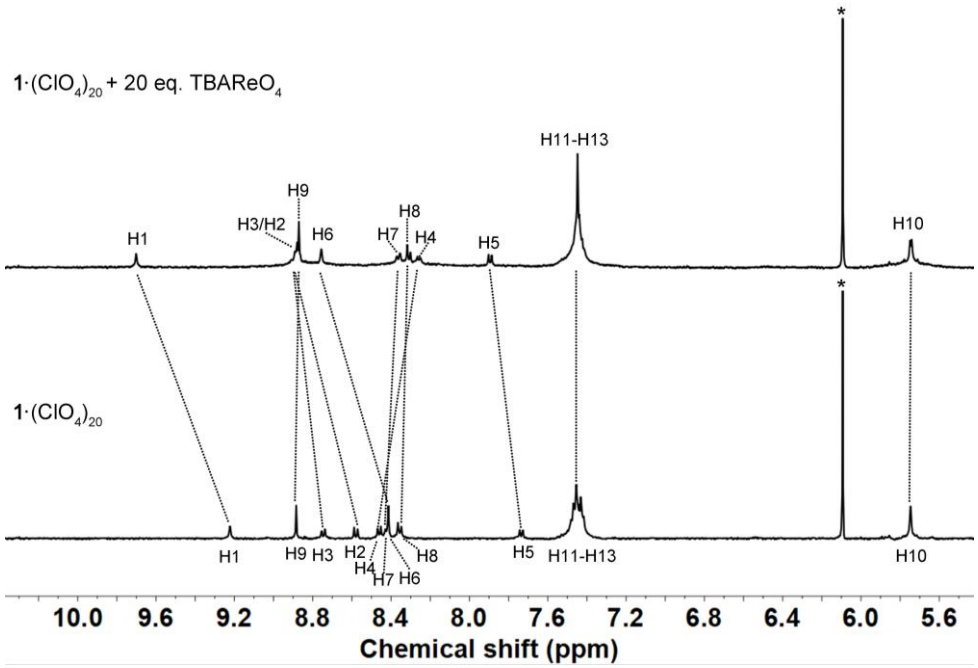

Figure S28. ^{1}H NMR spectra (CD_3CN, 500 MHz, 298 K) of **1**·$(ClO_4)_{20}$ (c = 11 μM) and **1**·$(ClO_4)_{20}$ following addition of 20 equiv. of $TBAReO_4$. The phenyl peak of the internal standard 1,3,5-trimethoxybenzene is indicated by an asterisk.

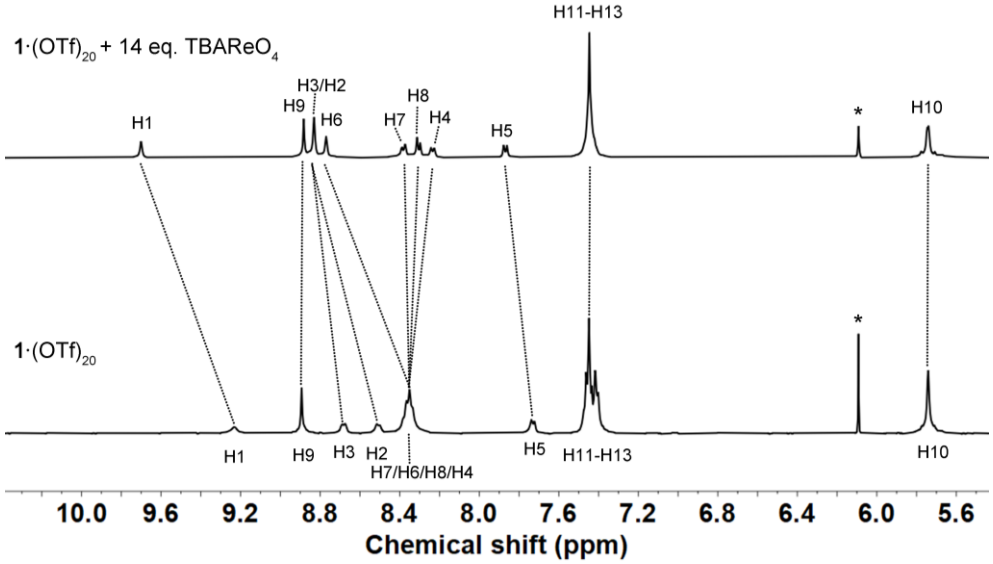

Figure S29. ^{1}H NMR spectra (CD_3CN, 500 MHz, 298 K) of **1**·$(OTf)_{20}$ (c = 71 μM) and **1**·$(OTf)_{20}$ with addition of 14 equiv. of $TBAReO_4$. The phenyl peak of the internal standard 1,3,5-trimethoxybenzene is indicated by an asterisk.

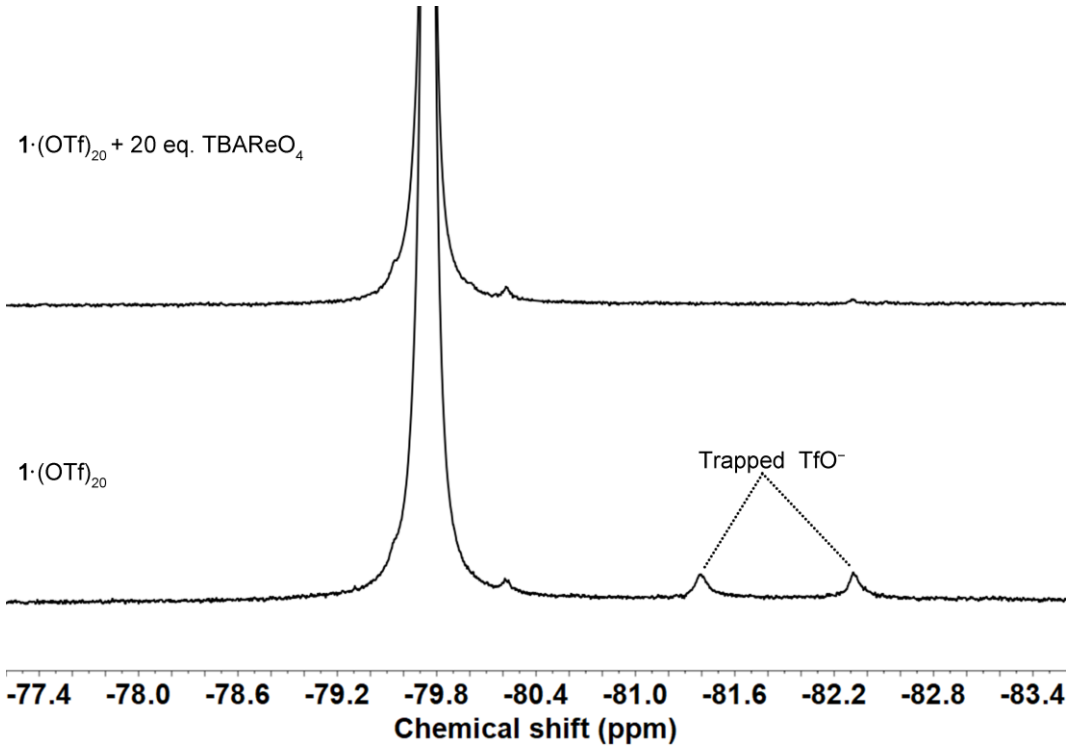

Figure S30. ^{19}F NMR spectra (CD_3CN, 470.4 MHz, 243 K) of **1**·$(OTf)_{20}$ (c = 75 μM) and **1**·$(OTf)_{20}$ with addition of 20 equiv. of $TBAReO_4$.

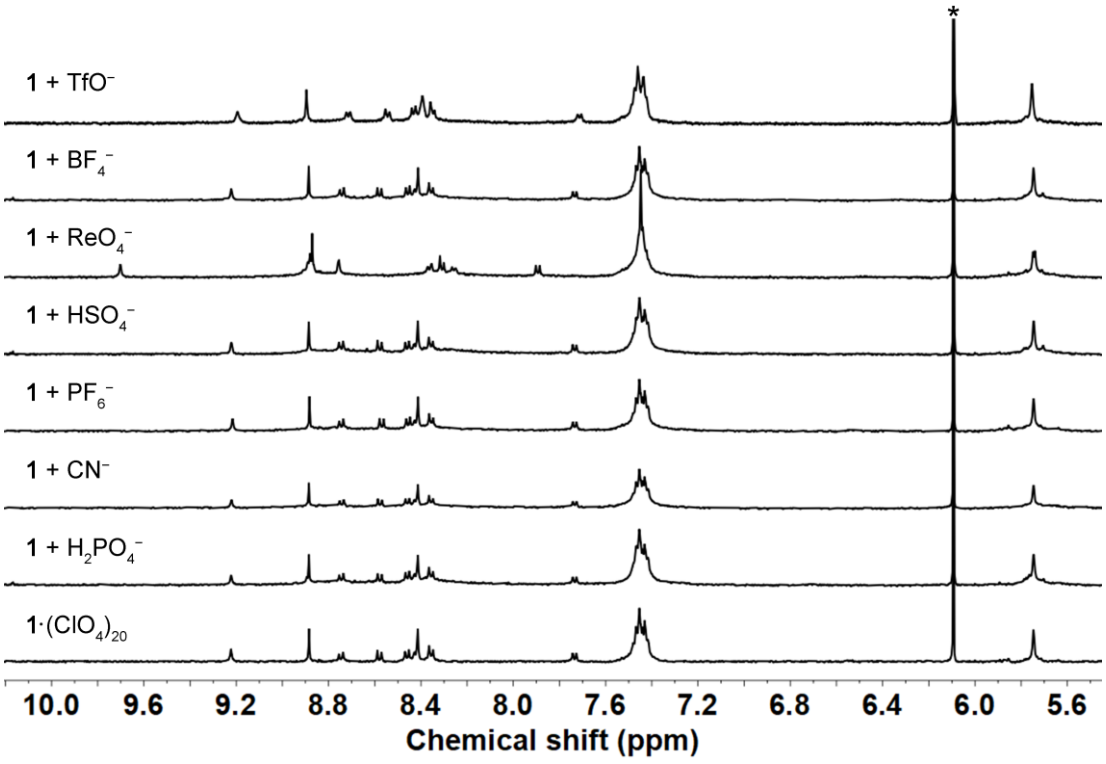

Figure S31. Partial ^1H NMR spectra (CD_3CN, 500 MHz, 298 K) of **1**·$(ClO_4)_{20}$ and **1** (12 μM) with addition of 20 equiv. different guest anions (added as their tetrabutylammonium (TBA^+) salts). The phenyl peak of the internal standard 1,3,5-trimethoxybenzene is indicated by an asterisk.

Table S1. Chemical shifts of imine (H1) and phenyl (H2-H5) ^{1}H NMR peaks of **1**·$(ClO_4^-)_{20}$ (12 μM in acetonitrile) with different prospective anion guests (20 equiv per **1**).

Guest	H1	H2	H3	H4	H5
ClO_4^-	9.223	8.571	8.737	8.452	7.727
$H_2PO_4^-$	9.222	8.570	8.736	8.451	7.726
NC^-	9.221	8.569	8.735	8.450	7.726
PF_6^-	9.216	8.561	8.736	8.447	7.726
HSO_4^-	9.221	8.570	8.737	8.452	7.726
ReO_4^-	9.702	8.880*	8.880*	8.250	7.886
BF_4^-	9.221	8.571	8.734	8.449	7.726
TfO^-	9.194	8.536	8.707	8.423	7.704

* The peaks could not be distinguished due to signal overlap.

S3.1.2 2D NMR

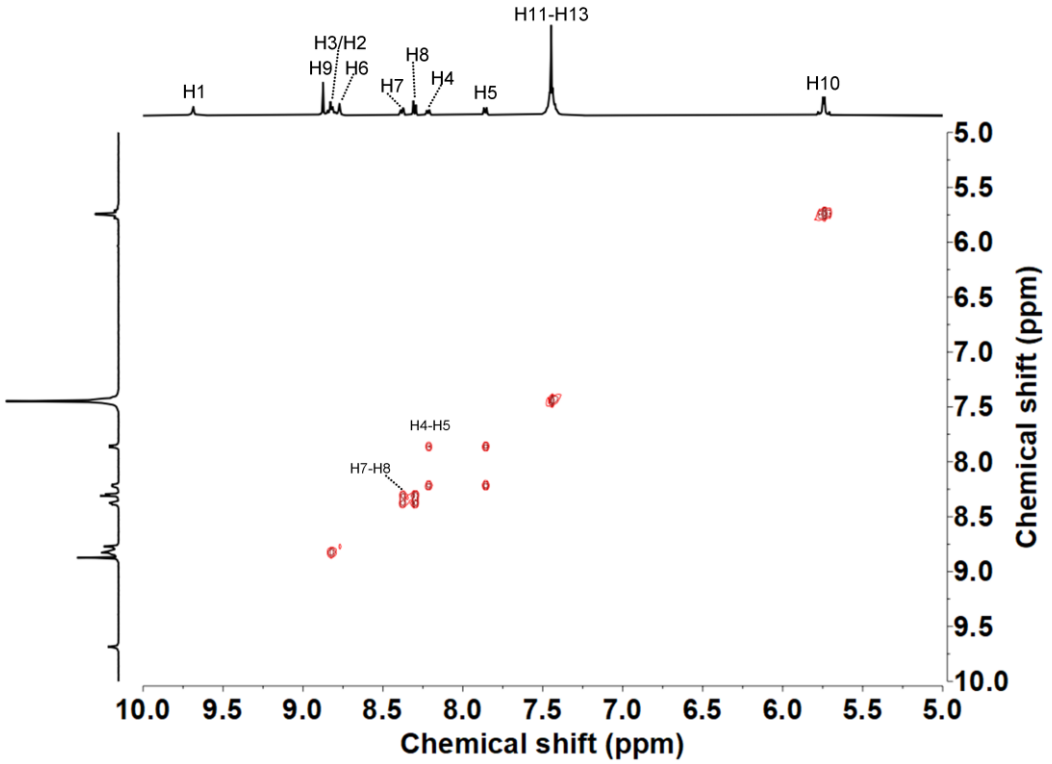

Figure S32. ^{1}H-^{1}H COSY (CD_3CN, 500 MHz, 298 K) of **1**·$(ReO_4)_{20}$

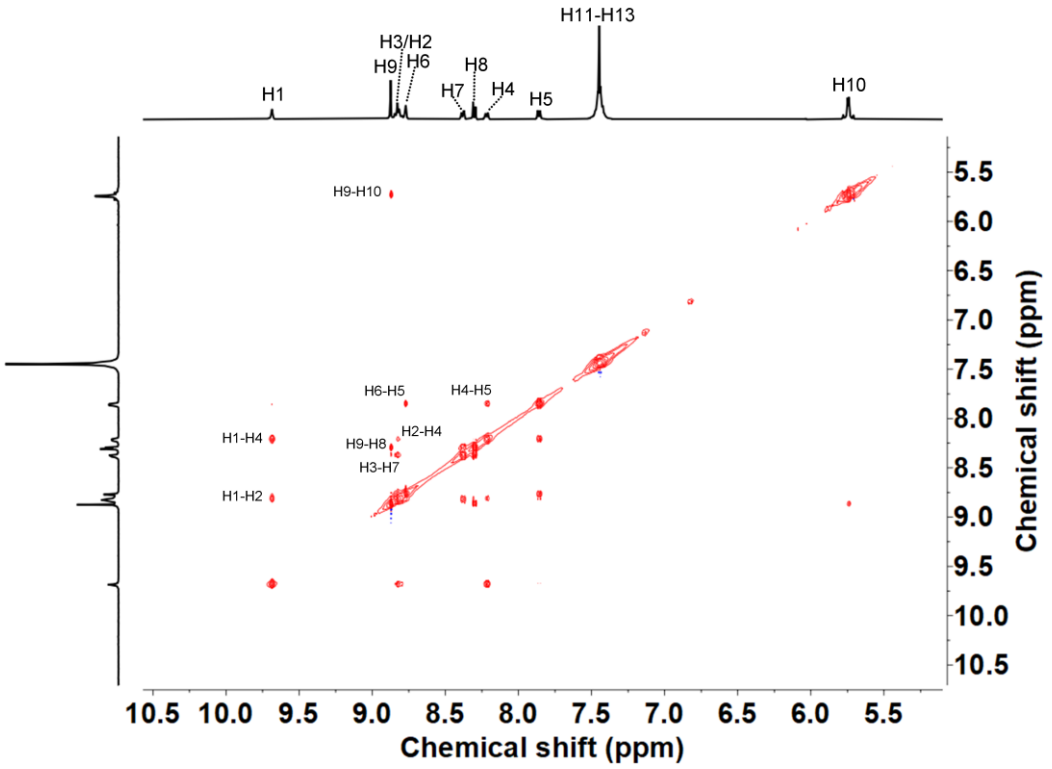

Figure S33. ^{1}H-^{1}H NOESY (CD_3CN, 500 MHz, 298 K) of **1**·$(ReO_4)_{20}$

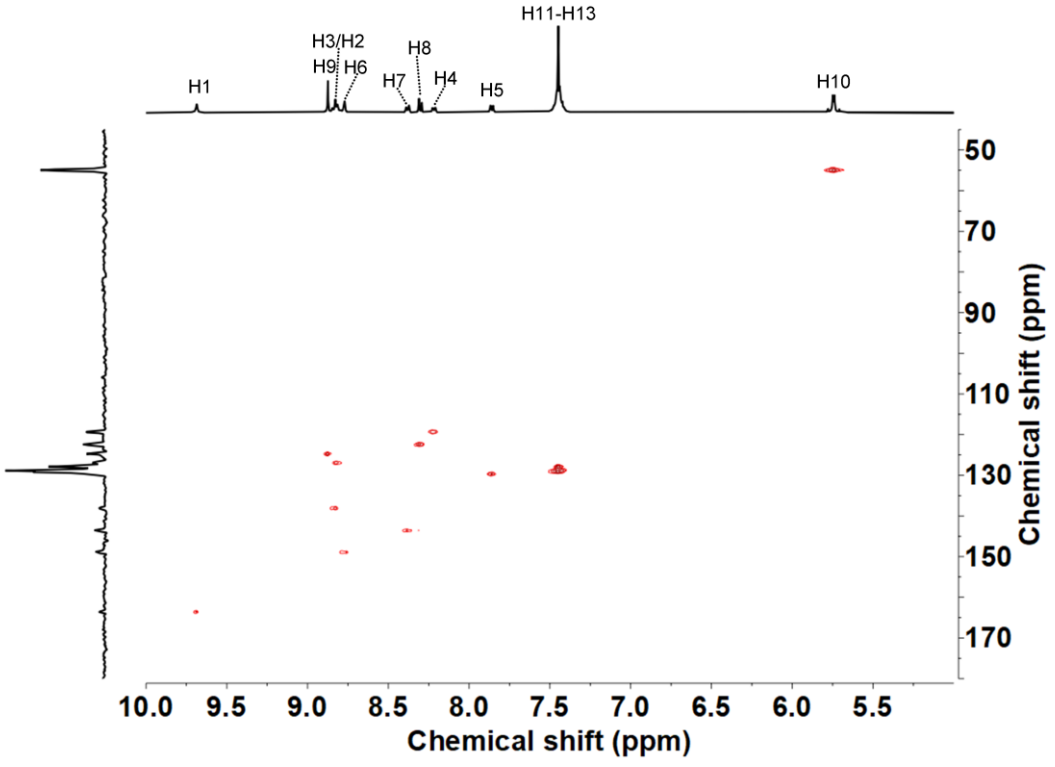

Figure S34. ^{1}H-^{13}C HSQC (CD_3CN, 500 MHz, 298 K) of **1**·$(ReO_4)_{20}$

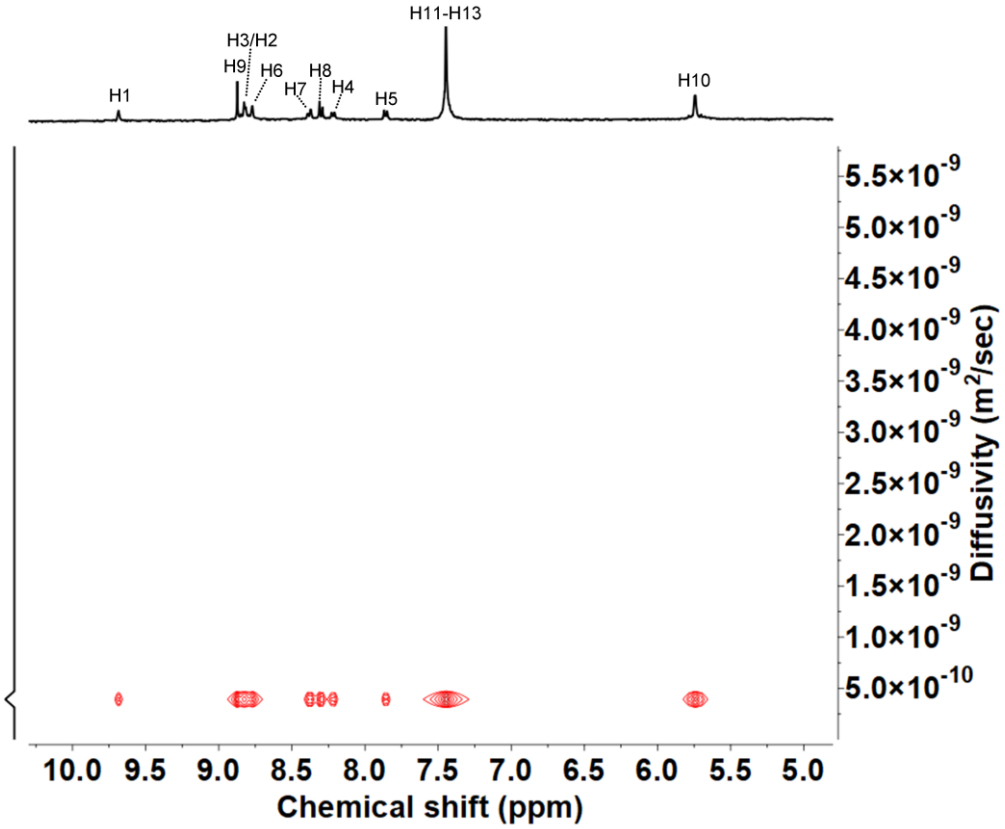

Figure S35. ^{1}H DOSY spectrum (CD_3CN, 400 MHz, 298 K) of **1**·$(ReO_4)_{20}$. The diffusion coefficient of **1**·$(ReO_4)_{20}$ in CD_3CN was measured to be 3.9×10^{-10} $m^2 \cdot s^{-1}$

S3.1.3 ESI-mass spectrum of 1 with ReO_4^- anions

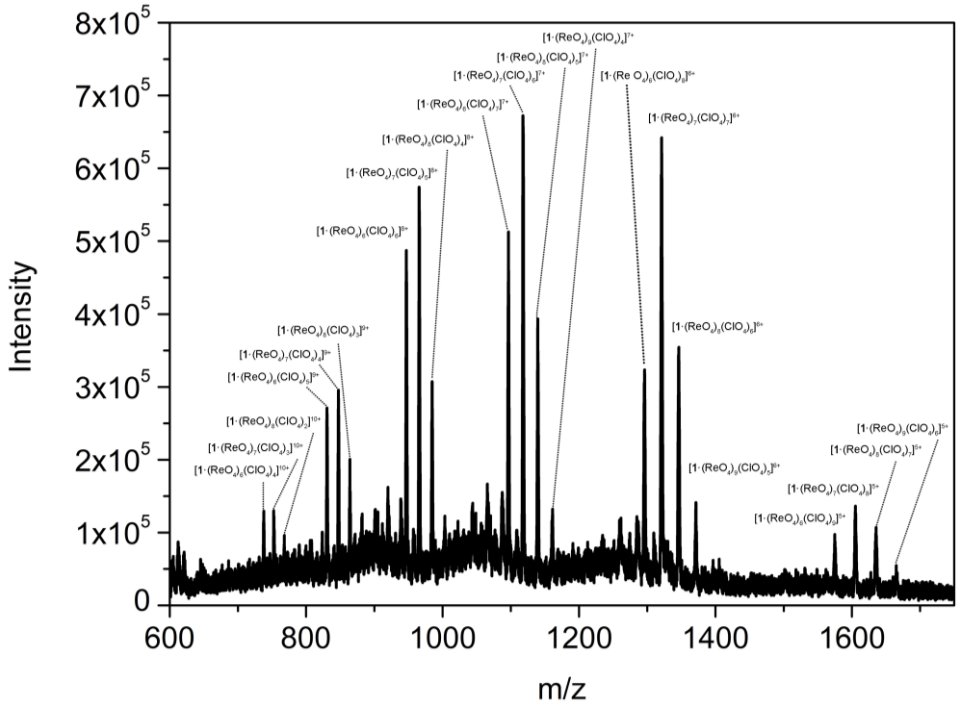

Figure S36. Low-resolution ESI-mass spectrometry analysis of **1**·$(ClO_4)_{20}$ with $TBAReO_4$.

S3.2 Apparent association constant of 1 with different anions

The binding behavior of capsule **1** was studied by competitive ^{1}H NMR titration of ReO_4^-, ClO_4^- and TfO^- into solutions of **1**·$(ClO_4)_{20}$ and **1**·$(OTf)_{20}$, respectively. Titration experiments of ReO_4^-, ClO_4^- and TfO^- were carried out in CD_3CN. The CD_3CN stock solution of **1**·$(ClO_4)_{20}$ and **1**·$(OTf)_{20}$ with an internal standard of 1,3,5-trimethoxybenzene (0.25 mM) were prepared. Stock solutions of $TBAReO_4$ (0.015 M), $TBAClO_4$ (0.75 M and 0.075 M) and TBAOTf (0.15 M) were also prepared and used for the titrations. The ^{1}H NMR titration were performed by adding aliquots of guest stock solution to 500 μL of **1** stock solution. It was found that ReO_4^- was bound by **1** in slow-exchange on the NMR time scale at 25 °C, while ClO_4^- and TfO^- interacted with **1** in a fast-exchange process.

The binding constant (K_a) and coefficient value (n) were calculated using the Hill equation.[5]

$$\theta = \frac{[HG_n]}{[HG_n] + [H]} \tag{S1}$$

$$\log\frac{\theta}{1 - \theta} = n\log[G] + n\log K_a \tag{S2}$$

Where θ is the fraction of binding sites occupied by the guest, [G] is the guest concentration, n is the Hill coefficient describing cooperativity, and K_a is the apparent association constant.

In the Hill equation, the value of θ was obtained using Equation S1. For the slow-exchange bound guest (ReO_4^-), according to the integration of the NMR peak of H1, the concentrations of the free host [H] and host-guest complex [HG] were determined, respectively. For the fast-exchange bound guests (ClO_4^- and TfO^-), the value of θ was obtained by using $\Delta\delta_{observed}$ as compared against the maximum change of chemical shift $\Delta\delta$ of H3 or H2 in ^{1}H NMR spectra.

Cooperativity is quantified by the Hill coefficient n, where $n > 1$ indicates positively cooperative binding, $n < 1$ indicates negatively cooperative binding, and $n = 1$ indicates noncooperative binding.

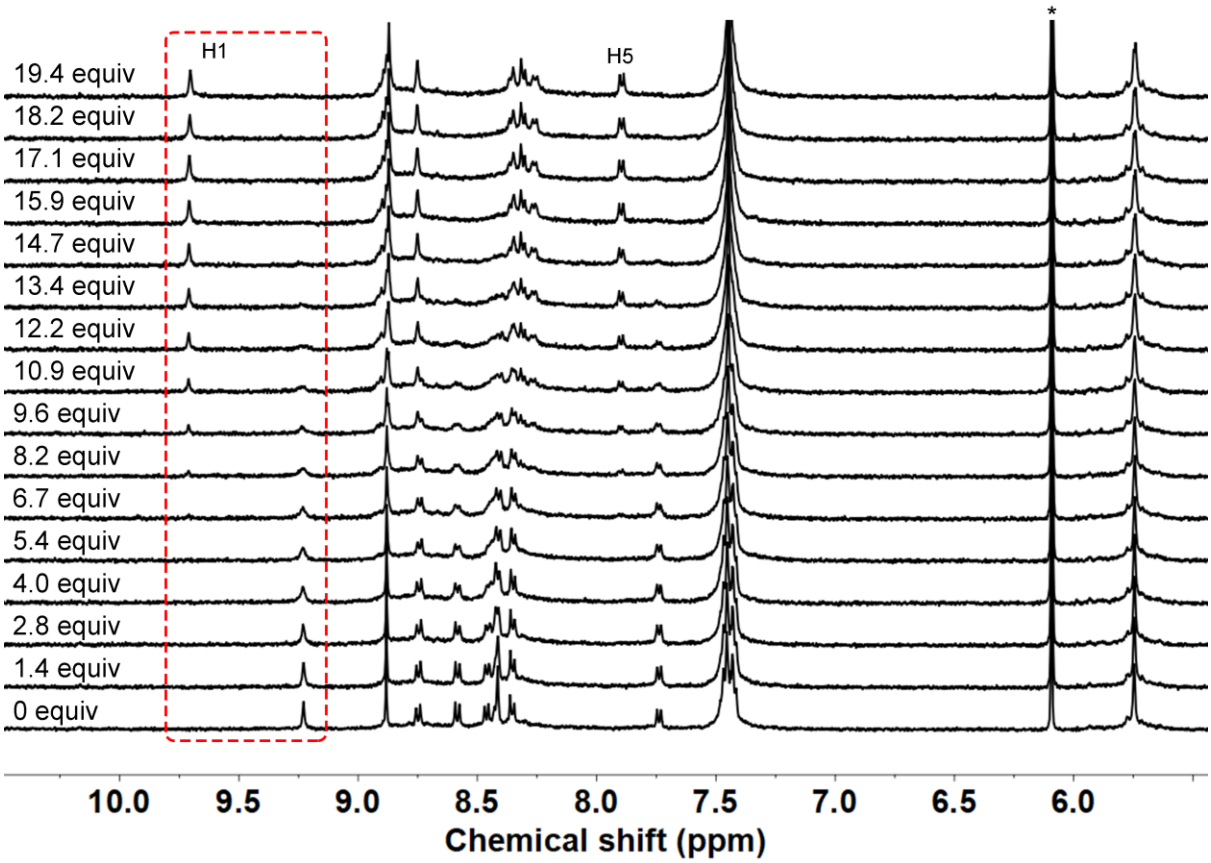

Figure S37. ^{1}H NMR spectra (CD_3CN, 500 MHz, 298 K) of **1**·$(ClO_4)_{20}$ (c = 11 μM) upon addition of 0 – 19.4 equiv of $TBAReO_4$. Imine protons H1 are highlighted in the red box. Guest equivalents with respect to the host are given on the left. The phenyl peak of the internal standard 1,3,5-trimethoxybenzene is indicated by an asterisk.

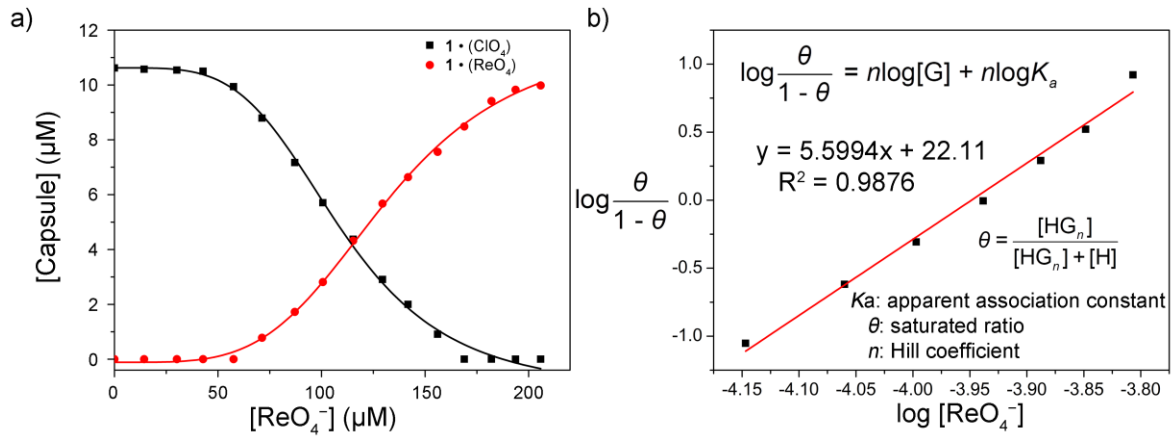

Figure S38. Titration curves of **1**·$(ClO_4)_{20}$ *vs* $TBAReO_4$ with Hill function. (a) [Capsule] *vs* [ReO_4^-] and (b) $\log\frac{\theta}{1-\theta}$ *vs* log[ReO_4^-].

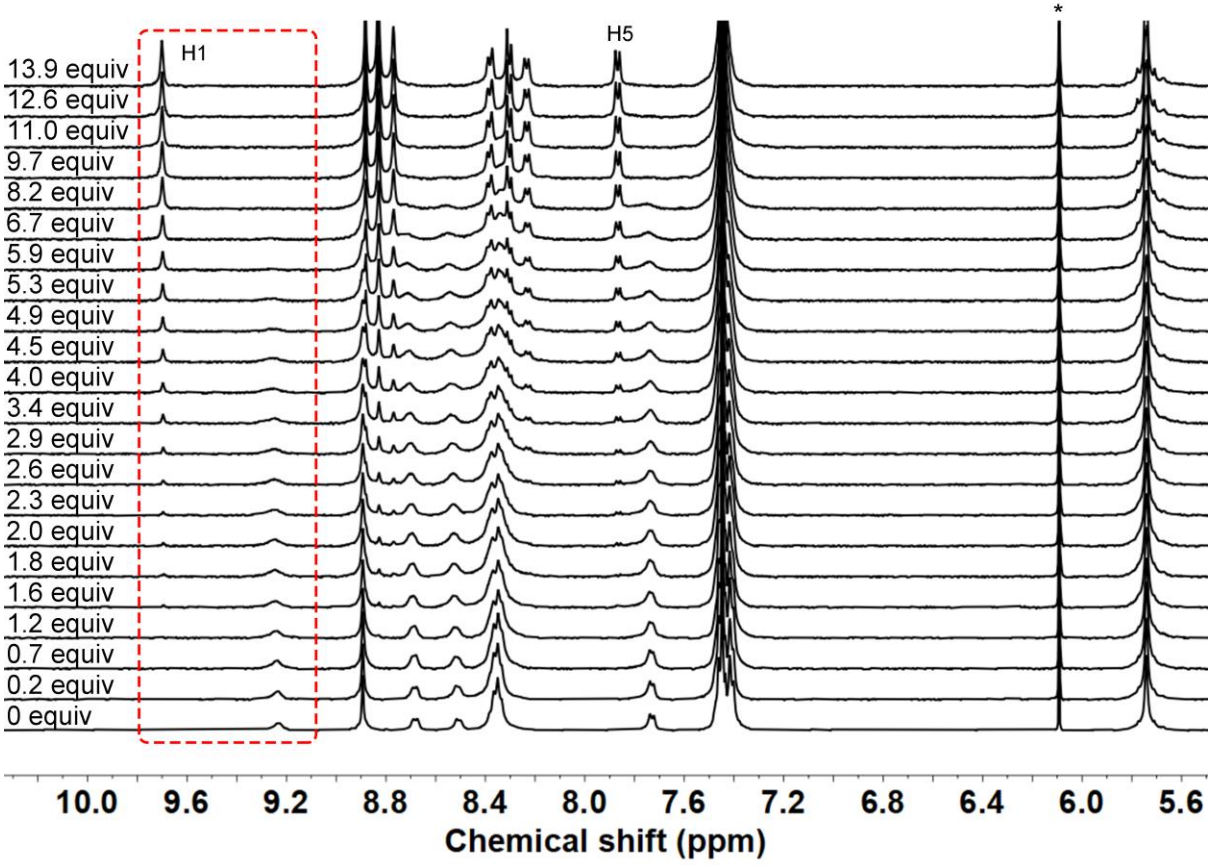

Figure S39. ^{1}H NMR spectra (CD_3CN, 500 MHz, 298 K) of **1**·$(OTf)_{20}$ (c = 70 μM) upon progressive addition of 13.9 equiv of $TBAReO_4$. Imine protons H1 are highlighted in red box. Guest equivalents with respect to the complete host are given on the left. The phenyl peak of the internal standard 1,3,5-trimethoxybenzene is indicated by an asterisk.

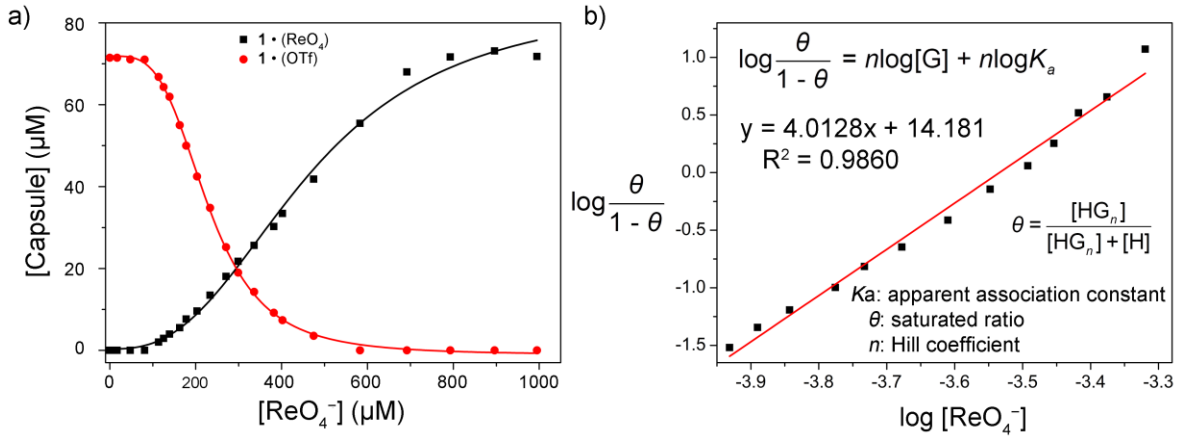

Figure S40. Titration curves of **1**·$(OTf)_{20}$ *vs* $TBAReO_4$ with Hill function. (a) [Capsule] *vs* [ReO_4^-] and (b) $\log\frac{\theta}{1-\theta}$ *vs* log[ReO_4^-].

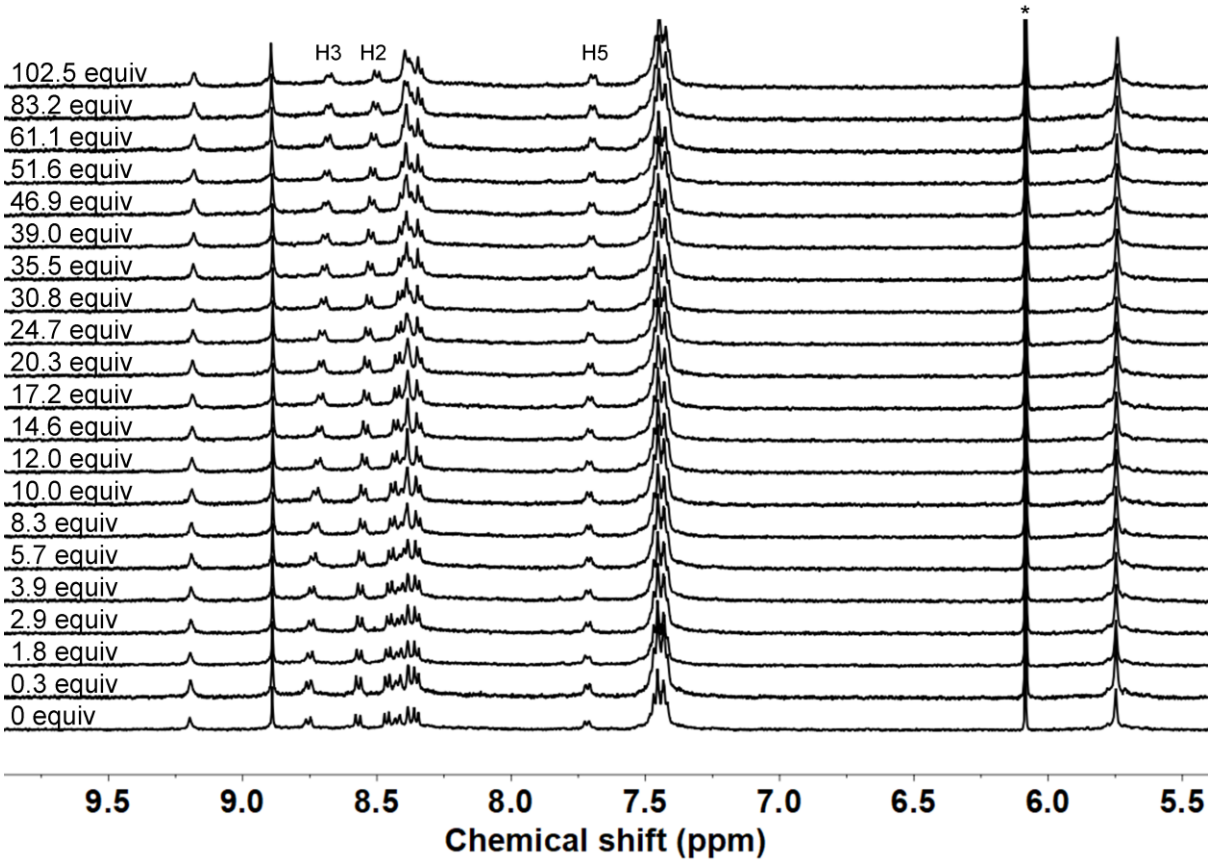

Figure S41. ^{1}H NMR spectra (CD_3CN, 500 MHz, 298 K) of **1**·$(ClO_4)_{20}$ (c = 16 μM) upon addition of 0 – 102.5 equiv of TBAOTf. Guest equivalents with respect to the complete host are given on the left. The phenyl peak of the internal standard 1,3,5-trimethoxybenzene is indicated by an asterisk.

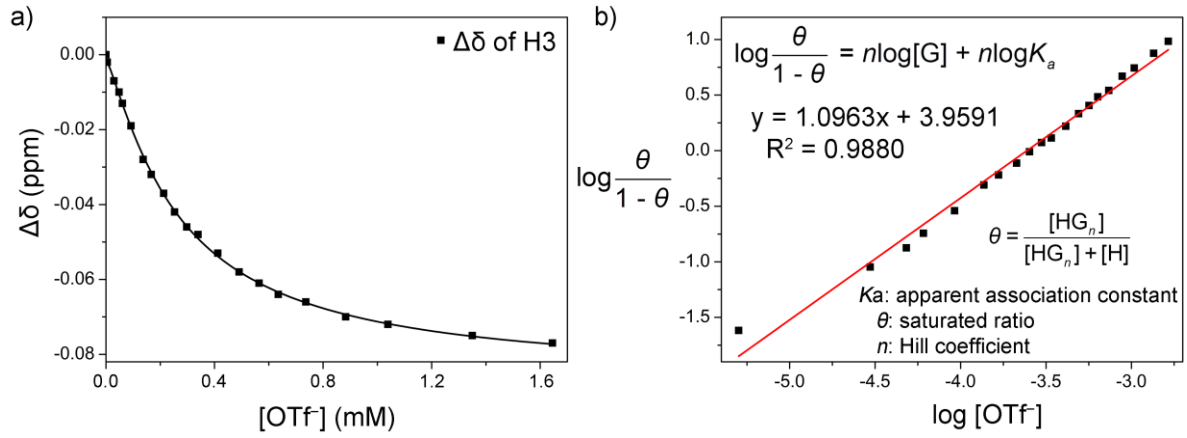

Figure S42. Titration curves of 1·$(ClO_4)_{20}$ *vs* TBAOTf with Hill function. (a) Δδ *vs* [TfO^-] and (b) $\log\frac{\theta}{1-\theta}$ *vs* log[TfO^-].

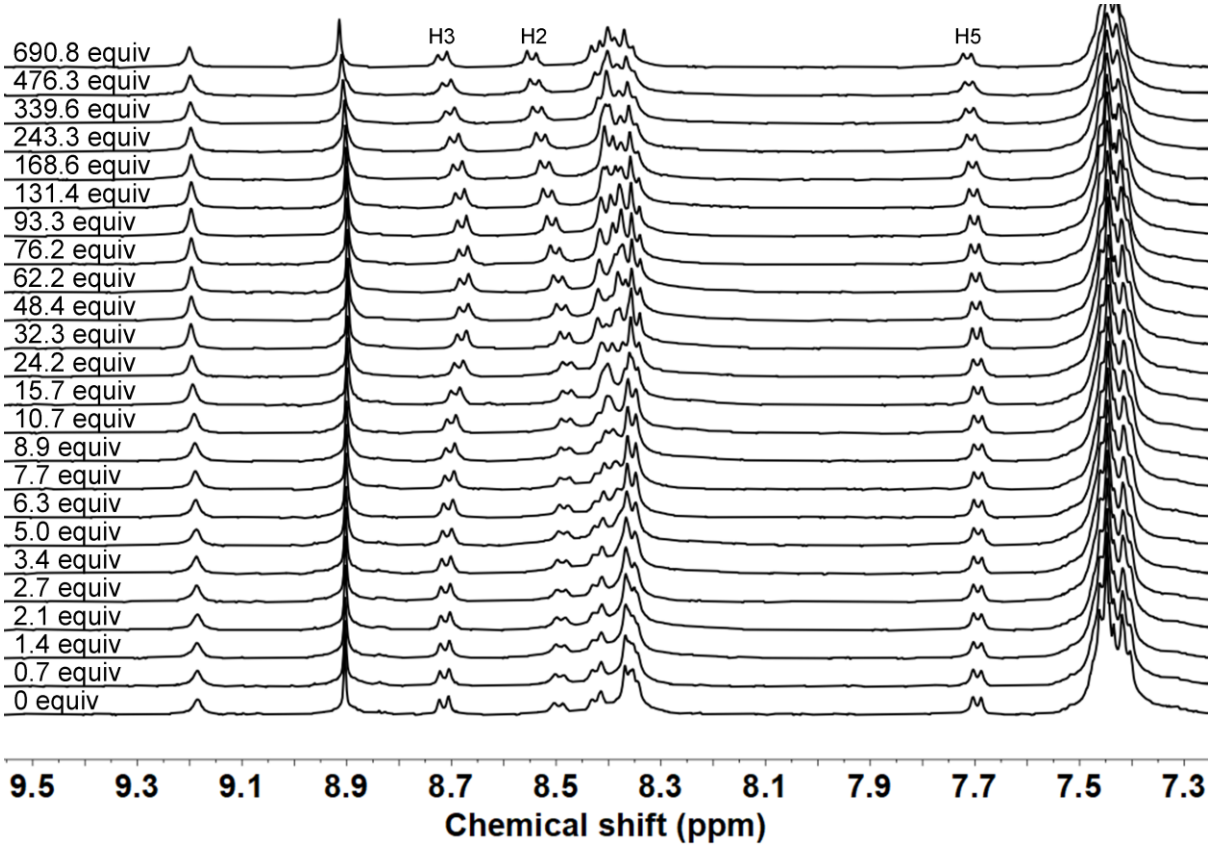

Figure S43. ^{1}H NMR spectra (CD_3CN, 500 MHz, 298 K) of **1**·$(OTf)_{20}$ (c = 48 μM) upon addition of 0 – 690.8 equiv of $TBAClO_4$. Guest equivalents with respect to the complete host are given on the left.

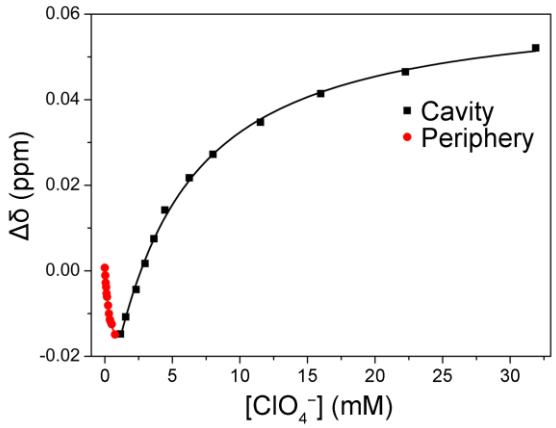

Figure S44. Titration curves of **1**·$(OTf)_{20}$ *vs* $TBAClO_4$ (Δδ of H2 *vs* $[ClO_4^-]$), showing initial peripheral binding and subsequent binding within the cavity.

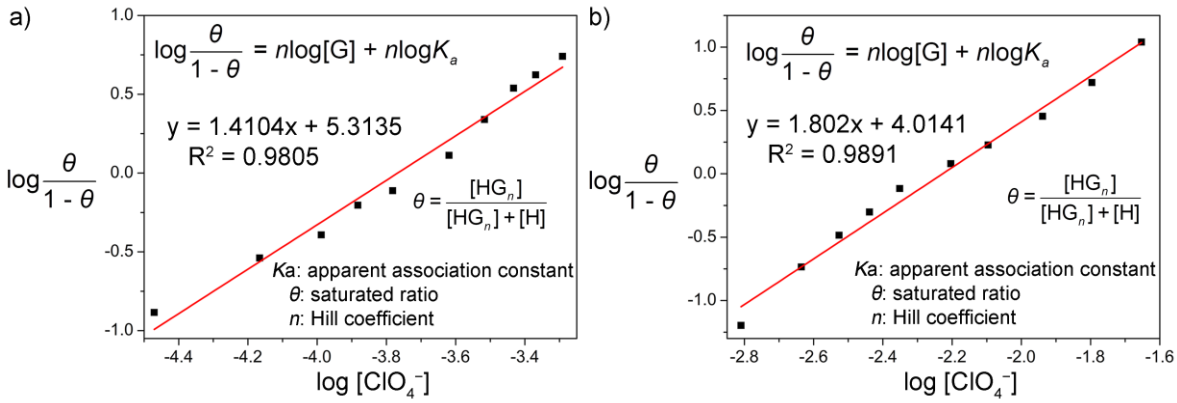

Figure S45. Titration data of **1**·$(OTf)_{20}$ *vs* $TBAClO_4$ with Hill function ($\log\frac{\theta}{1-\theta}$ *vs* log[ClO_4^-]). (a) From 0 equiv to 15.7 equiv and (b). From 15.7 equiv to 690.8 equiv.

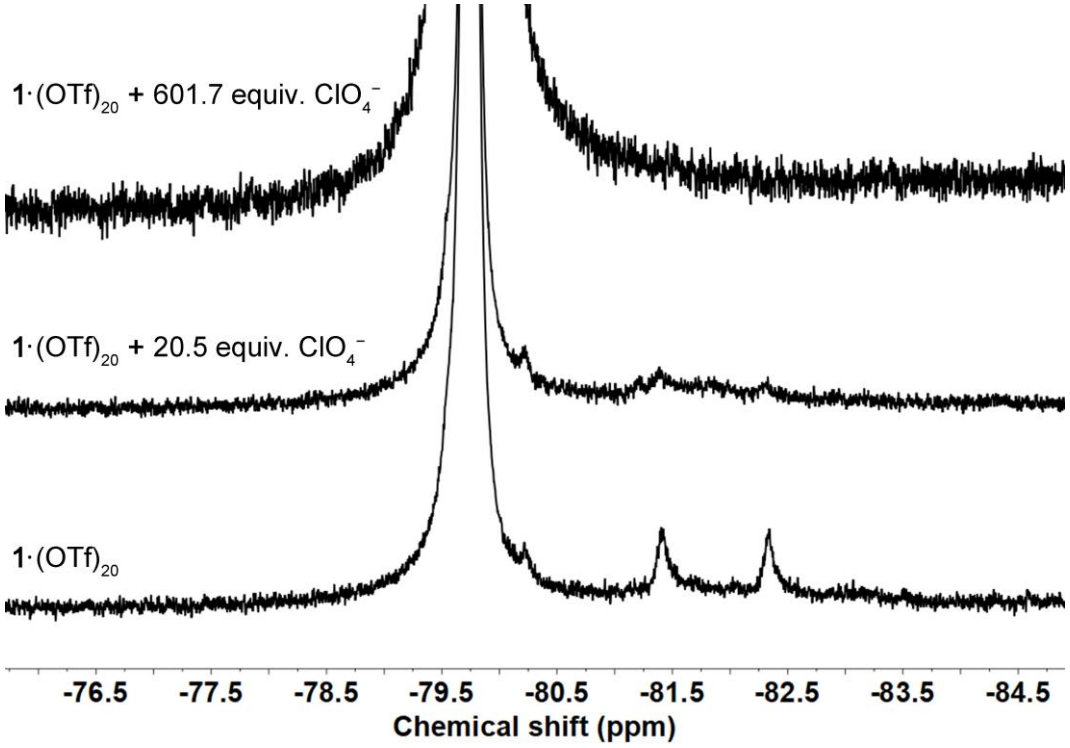

Figure S46. ^{19}F NMR spectra (CD_3CN, 470.4 MHz, 243 K) of **1**·$(OTf)_{20}$ and **1**·$(OTf)_{20}$ upon addition of 20.5 and 601.7 equiv. of $TBAClO_4$.

Interpretation of titration of ClO_4^- to 1·$(OTf)_{20}$

As observed in ^1H NMR titration of OTf^- into **1**·$(ClO_4)_{20}$, replacement of ClO_4^- by OTf^- occurs in a non-cooperative fashion (Figures S41, S42). Hence, OTf^- binds more strongly in the cage cavity than ClO_4^-. The stronger binding of OTf^- compared to ClO_4^- indicates that the reverse process, *i.e.* the titration of ClO_4^- to **1**·$(OTf)_{20}$, will require a large excess of ClO_4^- for displacement to occur, in line with LeChatelier's

principle. This outcome was observed when we added a large excess of ClO_4^-, as can be seen by the expected downfield shift of protons H2 and H3 (Figure S13) at higher ClO_4^- concentrations (Figures S43, S44) as well as by low-temperature ^{19}F NMR (243 K, Figure S46). In low-temperature ^{19}F NMR, the ^{19}F signals corresponding to encapsulated TfO^- disappeared only after the addition of a large excess (601.7 equiv) of ClO_4^-.

The interesting part of the titration of ClO_4^- to **1**·$(OTf)_{20}$ (Figures S43, S44) is the initially observed upfield shift of protons H2 and H3. The chemical shifts of H2 and H3 in **1**·$(ClO_4)_{20}$ compared to **1**·$(OTf)_{20}$ are at slightly higher chemical shift values (Figure S13). However, a replacement of TfO^- by ClO_4^- inside the cage's cavity would be indicated by a downfield shift of these signals. The observed upfield shift, thus, indicated a different kind of interaction. As there are six ClO_4^- anions located at the edges of **1** in the crystal structure (Figure S53), we hypothesize that the ClO_4^- interacts with the edges of the cage through electrostatic interactions and C-H···O hydrogen bonding in solution state.

S4. Spectroscopic properties

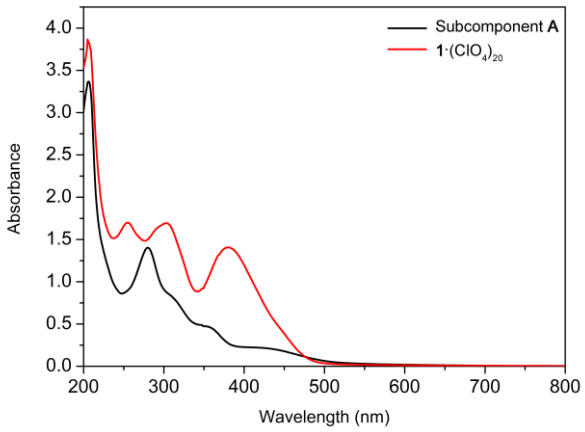

Figure S47. a) Ultraviolet–visible (UV-vis) spectra of **1**·$(ClO_4)_{20}$ (2 μM in MeCN) and subcomponent **A** (24 μM in MeCN).

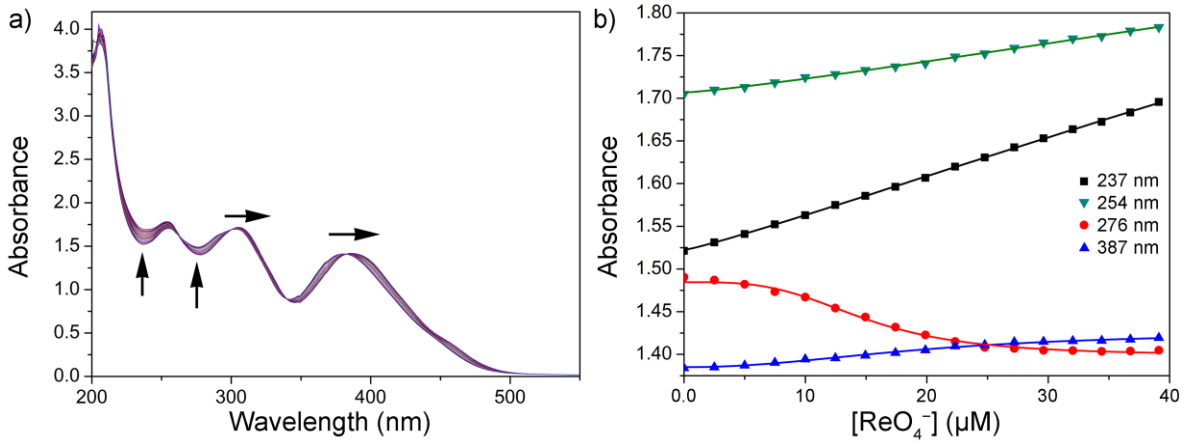

Figure S48. a) Ultraviolet–visible (UV-vis) spectra of **1**·$(ClO_4)_{20}$ (2 μM in MeCN) upon progressive addition of 19.5 equiv. of $TBAReO_4$. b) Variation of absorbance at four different wavelengths.

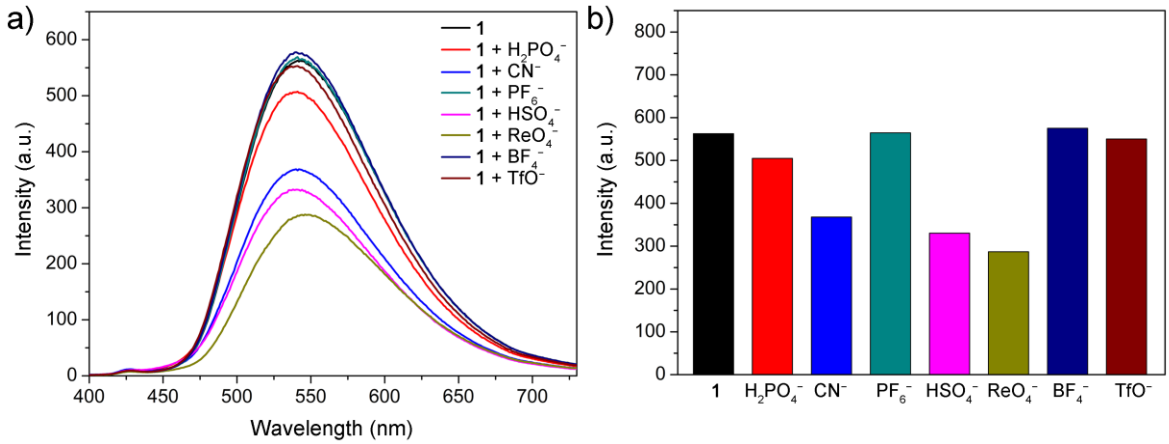

Figure S49. a) Fluorescence emission spectra of **1**·$(ClO_4)_{20}$ (2 μM in MeCN, λ_{ex}=375 nm) upon addition of various anions (20 equiv); b) Variation of fluorescence intensity at λ =543 nm.

S5. X-ray Crystallography

Data were collected at Beamline I19 of Diamond Light Source employing silicon double crystal monochromated synchrotron radiation (0.6889 Å) with ω and ψ scans at 100(2) K.[6] Data integration and reduction were undertaken with Xia2.[7] Subsequent computations were carried out using the WinGX-32 graphical user interface.[8] Multi-scan empirical absorption corrections were applied to the data using the AIMLESS[9] tool in the CCP4 suite[10] or DIALS.[11] The structures were solved by direct methods using SHELXT[12] then refined and extended with SHELXL.[13] In general, non-hydrogen atoms with occupancies greater than 0.5 were refined anisotropically. Carbon-bound hydrogen atoms were included in idealised positions and refined using a riding model. Oxygen-bound hydrogen atoms were first located in the difference Fourier map before refinement. Disorder was modelled using standard crystallographic methods

including constraints and restraints where necessary. Crystallographic data have been deposited with the CCDC (CCDC 2024202).

Crystals of $[Zn_4La_4L_4(H_2O)_{12}]\cdot 20ClO_4\cdot 3H_2O$ were grown by vapour diffusion of diethyl ether into an acetonitrile solution of the complex. The crystals employed in this study proved to be weakly diffracting and rapidly suffered solvent loss. Rapid handling prior to quenching in liquid nitrogen was required to collect data. Despite these measures and the use of synchrotron radiation the diffraction pattern was broad and the intensity of reflections dropped off rapidly past 1 Å. The tetrahedral assembly crystallised in the space group I23 and was refined as a merohedral twin. The absolute configuration of the crystal could not be determined reliably but we assume the bulk sample is racemic. The capsule shows a high degree of crystallographic symmetry with 1/12 of the tetrahedron in the asymmetric unit.

Due to the less than ideal resolution and thermal motion present in the structure restraints were applied to the organic part of the structure to achieve a reasonable refinement. The GRADE program[14] was employed using the GRADE Web Server[15] to generate a full set of bond distance and angle restraints (DFIX, DANG, FLAT) for the ligand and thermal parameter restraints (SIMU, RIGU) were applied to all atoms except for zinc, lanthanum and chlorine.

The anions within the structure show evidence of substantial disorder. The encapsulated perchlorate anion was modelled over two locations, each located on a site of 3-fold symmetry. A further perchlorate anion was located outside the capsule and modelled with partial occupancy. Bond length restraints were applied to both located perchlorate anions. Hydrogen atoms were not applied to one water molecule located on a special position.

Further reflecting the solvent loss and poor diffraction properties there is a significant amount of void volume in the lattice containing smeared electron density from disordered solvent and 13 unresolved anions per $Zn_4La_4L_4$ tetrahedron (included as perchlorate in the formula). Consequently the SQUEEZE[16] function of PLATON[17] was employed to remove the contribution of the electron density associated with these remaining anions and further highly disordered solvent, which gave a potential solvent accessible void of 10406 $Å^3$ per unit cell (a total of approximately 3086 electrons). Diffuse solvent molecules could not be assigned to acetonitrile or diethyl ether and were therefore not included in the formula. Consequently, the molecular weight and density given above are underestimated.

CheckCIF gives 3 A level alerts for short inter D···A contact generated in error for oxygen atoms part

of a single perchlorate anion located on a special position. One B level alert for low bond precision on C-C bonds arises from the limited resolution of the data (and low intensity of high angle data) and two further B alerts for short inter D···A contacts arise from an the water molecule located on a special position for which hydrogen atoms were not modelled.

Table S2. Crystal data and refinement details of tetrahedral **1** • $(ClO_4^-)_{20}$

	1
Empirical formula	$C_{288}H_{230}Cl_{20}La_4N_{72}O_{99}Zn_4$
Formula weight	7809.55
Crystal System	Cubic
Space group	I23
a (Å)	28.2940(2)
b (Å)	28.2940(2)
c (Å)	28.2940(2)
α (deg)	90
β (deg)	90
γ (deg)	90
V (Å^3)	22650.8(5)
Z	2
$D_{calc,}$ g/cm^3	1.145
No. of unique data	7746
T (K)	100(2)
Total no. of data	75589
Crystal size (mm)	0.050 x 0.050 x 0.030
θ range	0.986 to 25.494°
Completeness to *θ* = 24.415°	100 %
Max. and min. transmission	1.0 and 0.9744
Goodness-of-fit on F^2	0.986
*R*1	0.0736
*wR*2	0.1868

*$R1 = \Sigma||F_o| - |F_c||/\Sigma|F_o|$ for $F_o > 2\sigma(F_o)$; $wR2 = (\Sigma w(F_o^2 - F_c^2)^2/\Sigma(wF_c^2)^2)^{1/2}$ all reflections

$w=1/[\sigma^2(F_o^2)+(0.1484P)^2]$ where $P=(F_o^2+2F_c^2)/3$

Table S3. Hydrogen bonds between capsules.

D−H···A	*d*(D−H)	*d*(H···A)	*d*(D···A)	∠(DHA)
O2−H2A···N2	0.88	2.41	3.2662(1)	165
O2−H2B···N2	0.88	2.44	2.8627(1)	110

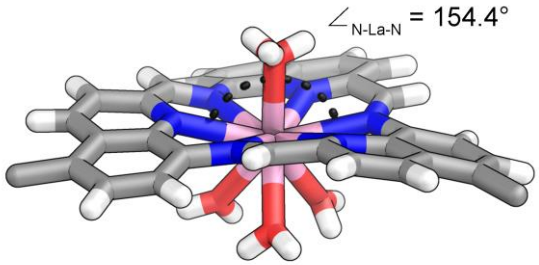

Figure S50. Structure of bowl-like central spacer of the C_3 symmetric ligand. The N-La-N angle between imine and quinoline donors which are opposite each other is marked to indicate the bent nature of the ligand. The top one of the water molecules is disordered over three sites by symmetry

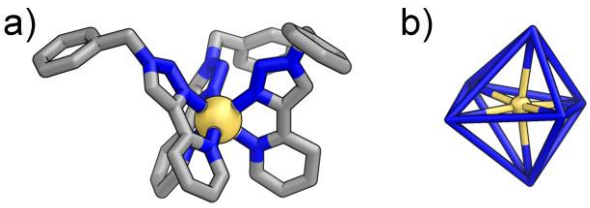

Figure S51. a) Coordination environment of the Zn^{II} cation. b) Side view of the coordination geometry of the Zn^{II} cation.

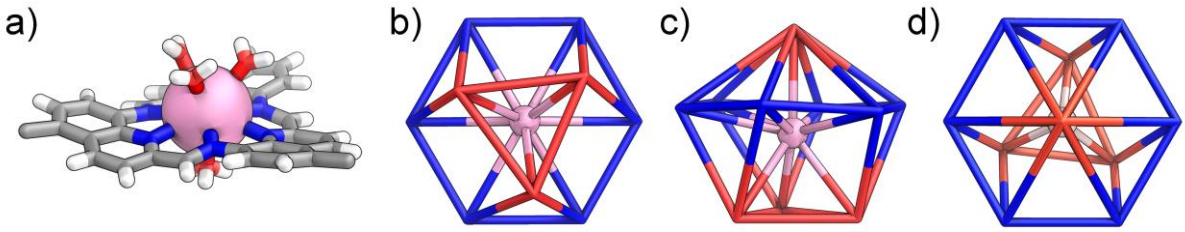

Figure S52. a) Coordination environment of the La^{III} cation. b), c) and d) are the top, side and bottom views of coordination geometry of La^{III} cation.

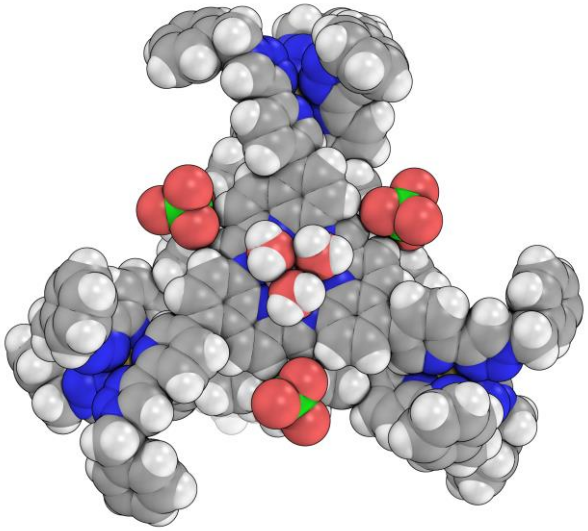

Figure S53. Crystal structure of **1**·$(ClO_4)_{20}$. Space-filling view showing three of the six peripheral ClO_4^- counter anions associated with **1**.

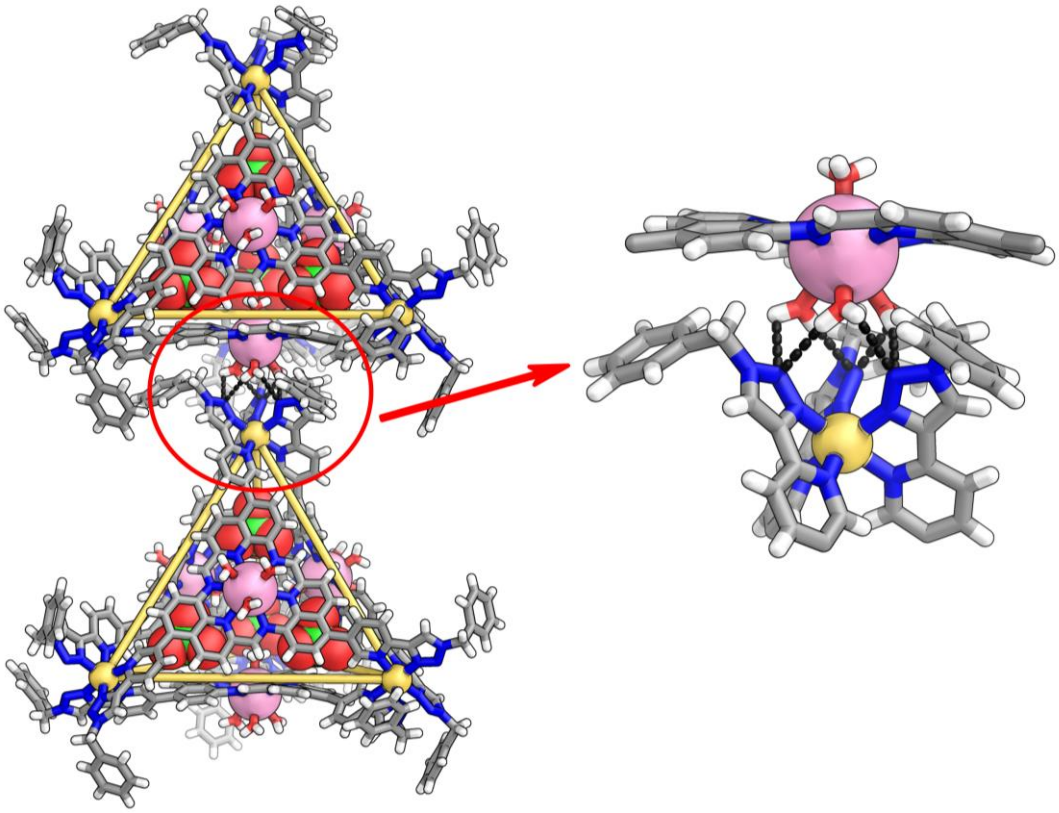

Figure S54. Intermolecular hydrogen bonds of **1**·$(ClO_4)_{20}$. The water molecules which are located inside the cavity are disordered over three sites by symmetry. Hydrogen bonds were formed between capsules. The outward-facing H_2O molecules coordinated to the Ln^{III} cations each were in hydrogen-bonding distance of the three triazole N atoms at a vertex of a neighboring capsule, with O···N distances of 3.27(2) and 2.86(2) Å.

S6. Volume calculations

In order to determine the available void space within **1**, VOIDOO calculations[18] based on the crystal structure (with the encapsulated anions and bound water molecules removed) was performed. A virtual probe with a radius of 1.4 Å (set by default, water-sized) was employed. The standard parameters tabulated below was used, following the previously published procedure.[19]

Maximum number of volume-refinement cycles: 30

Minimum size of secondary grid: 3

Grid for plot files: 0.2

Primary grid spacing: 0.1

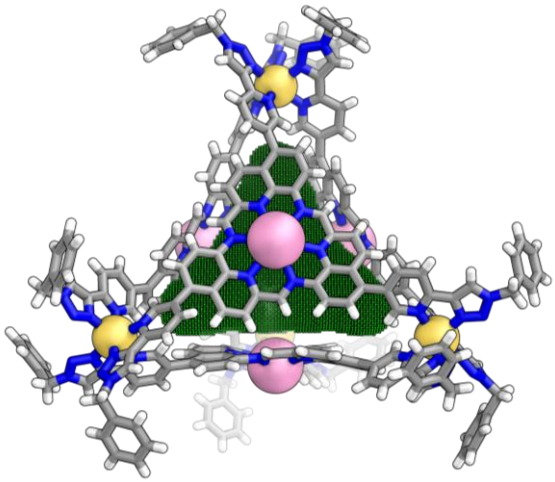

Figure S55. VOIDOO-calculated void space (green mesh) within the cavity of **1** (volume: 617.3 Å^3).

Reference:

1. Tilley, J. W.; Zawoiski, S., A Convenient Palladium-Catalyzed Coupling Approach to 2,5-Disubstituted Pyridines. *J. Org. Chem.* **1988,** *53*, 386-90.

2. Xue, G.; Bradshaw, J. S.; Dalley, N. K.; Savage, P. B.; Krakowiak, K. E.; Izatt, R. M.; Prodi, L.; Montalti, M.; Zaccheroni, N., Convenient Syntheses and Preliminary Photophysical Properties of Novel 8-Aminoquinoline Appended Diaza-18-crown-6 Ligands. *Tetrahedron* **2001,** *57*, 7623-7628.

3. Greenfield, J. L.; Di, A. M.; Nitschke, J. R.; Evans, E. W.; Di, N. D.; Friend, R. H., Unraveling Mechanisms of Chiral Induction in Double-Helical Metallopolymers. *J. Am. Chem. Soc.* **2018,** *140*, 10344-10353.

4. Shyshov, O.; Brachvogel, R.-C.; Bachmann, T.; Srikantharajah, R.; Segets, D.; Hampel, F.; Puchta, R.; von Delius, M., Adaptive Behavior of Dynamic Orthoester Cryptands. *Angew. Chem., Int. Ed.* **2017,** *56*, 776-781.

5. Takezawa, H.; Murase, T.; Resnati, G.; Metrangolo, P.; Fujita, M., Recognition of Polyfluorinated Compounds Through Self-Aggregation in a Cavity. *J. Am. Chem. Soc.* **2014,** *136*, 1786-1788.

6. Allan, D.; Nowell, H.; Barnett, S.; Warren, M.; Wilcox, A.; Christensen, J.; Saunders, L.; Peach, A.; Hooper, M.; Zaja, L.; Patel, S.; Cahill, L.; Marshall, R.; Trimnell, S.; Foster, A.; Bates, T.; Lay, S.; Williams, M.; Hathaway, P.; Winter, G.; Gerstel, M.; Wooley, R., A Novel Dual Air-Bearing Fixed-χ Diffractometer for Small-Molecule Single-Crystal X-ray Diffraction on Beamline I19 at Diamond Light Source. *Crystals* **2017,** *7*, 336.

7. (a) Bailey, S., The CCP4 suite: programs for protein crystallography. *Acta Crystallogr., Sect. D: Biol. Crystallogr.* **1994,** *D50*, 760-763; (b) Evans, P., Scaling and assessment of data quality. *Acta Crystallogr., Sect. D: Biol. Crystallogr.* **2006,** *D62*, 72-82; (c) Winter, G., xia2: An expert system for macromolecular crystallography data reduction. *J. Appl. Crystallogr.* **2010,** *43*, 186-190.

8. Farrugia, L., WinGX and ORTEP for Windows: an update. *J. Appl. Crystallogr.* **2012,** *45*, 849-854.

9. Evans, P. R.; Murshudov, G. N., How good are my data and what is the resolution? *Acta Crystallogr., Sect. D: Biol. Crystallogr.* **2013,** *69*, 1204-1214.

10. Winn, M. D.; Ballard, C. C.; Cowtan, K. D.; Dodson, E. J.; Emsley, P.; Evans, P. R.; Keegan, R. M.; Krissinel, E. B.; Leslie, A. G. W.; McCoy, A.; McNicholas, S. J.; Murshudov, G. N.; Pannu, N. S.; Potterton, E. A.; Powell, H. R.; Read, R. J.; Vagin, A.; Wilson, K. S., Overview of the CCP4 suite and current developments. *Acta Crystallogr., Sect. D: Biol. Crystallogr.* **2011,** *67*, 235-242.

11. Winter, G.; Waterman, D. G.; Parkhurst, J. M.; Brewster, A. S.; Gildea, R. J.; Gerstel, M.; Fuentes-Montero, L.; Vollmar, M.; Michels-Clark, T.; Young, I. D.; Sauter, N. K.; Evans, G., DIALS: implementation and evaluation of a new integration package. *Acta Crystallogr., Sect. D: Struct. Biol.* **2018,** *74*, 85-97.

12. Sheldrick, G. M., SHELXT - Integrated space-group and crystal-structure determination. *Acta Crystallogr., Sect. A: Found. Adv.* **2015,** *71*, 3-8.

13. Sheldrick, G. M., Crystal structure refinement with SHELXL. *Acta Crystallogr., Sect. C: Struct. Chem.* **2015,** *71*, 3-8.

14. Bricogne, G.; Blanc, E.; Brandle, M.; Flensburg, C.; Keller, P.; Paciorek, W.; Roversi, P.; Sharff, A.; Smart, O. S.; Vonrhein, C.; Womack, T. O., *BUSTER*. 2.11.2 ed.; Global Phasing Ltd.: Cambridge, United Kingdom, 2011.

15. Smart, O. S.; Womack, T. O., *Grade Web Server*. Global Phasing Ltd. : 2014.

16. Van der Sluis, P.; Spek, A. L., BYPASS: an effective method for the refinement of crystal structures containing disordered solvent regions. *Acta Crystallogr., Sect. A: Found. Crystallogr.* **1990,** *A46*, 194-201.

17. Spek, A. L., *PLATON: A Multipurpose Crystallographic Tool*. Utrecht University: Utrecht, The Netherlands, 2008.

18. Kleywegt, G. J.; Jones, T. A., Detection, delineation, measurement and display of cavities in macromolecular structures. *Acta Crystallogr., Sect. D: Biol. Crystallogr.* **1994,** *D50*, 178-85.

19. Hristova, Y. R.; Smulders, M. M. J.; Clegg, J. K.; Breiner, B.; Nitschke, J. R., Selective anion binding by a "Chameleon" capsule with a dynamically reconfigurable exterior. *Chem. Sci.* **2011,** *2*, 638-641.